Deformation-induced cleaning of organically fouled membranes: Fundamentals and techno-economic assessment for spiral-wound membranes

Deformation-induced cleaning of organically fouled membranes: Fundamentals and techno-economic assessment for spiral-wound membranes

Grace S. S. Goon[a,†], Omar Labban[b,†], Zi Hao Foo[b,c], Xuanhe Zhao [b,‡], John H. Lienhard V[b,‡*]

[a] *Department of Aeronautics and Astronautics, Massachusetts Institute of Technology, Cambridge MA 02139-4307, USA*

[b] *Department of Mechanical Engineering, Massachusetts Institute of Technology, Cambridge MA 02139-4307, USA*

[c] *School of Mechanical and Aerospace Engineering, Nanyang Technological University, Singapore 639798, Singapore*

[†] *Joint first authors.*

[‡] *Joint senior authors.*

Abstract

Membrane fouling is a ubiquitous challenge in water treatment and desalination systems. Current reverse osmosis (RO) membrane cleaning technology relies on chemical processes, incurring considerable costs and generating waste streams. Here, we present a novel chemical-free membrane cleaning method applicable to commercially existing RO spiral-wound membrane modules. The method employs controlled membrane deformation through pressure modulation, which induces shear stresses at the foulant-membrane interface that lead to detachment and removal of the foulants. To investigate the effectiveness of the method, experiments on organic fouling by alginate are conducted on a flat-sheet membrane coupon followed by tests on a commercial spiral-wound module with feeds of varying fouling propensities. Cleaning durations are six-fold lower, and the experimental results demonstrate flux recoveries and cleaning efficiencies comparable to those of chemical cleaning. The experiments on the spiral-wound module indicate that this method will have applicability in industrially-relevant settings. To elucidate the underlying cleaning mechanisms, membrane deformation experiments with no flow are conducted, and in situ visualization techniques are employed for both the flat-sheet and spiral-wound modules. The results show that cleaning is caused by a reduction in shear strength at the foulant-membrane interface after cycles of repeated loading, a behavior typical of fatigue. By enabling more frequent cleanings, deformation-induced cleaning is shown to considerably lower operating costs in an economic case study while offering a more sustainable and environmentally sound solution to membrane cleaning and antifouling in desalination.

Keywords: reverse osmosis, membrane fouling, chemical cleaning, chemical-free cleaning, deformation-induced cleaning.

*Corresponding author: lienhard@mit.edu

G. Goon, O. Labban, Z.H. Foo, X. Zhao, and J.H. Lienhard V, "Deformation-induced cleaning of organically fouled membranes: Fundamentals and techno-economic assessment for spiral-wound membranes," *J. Membrane Sci.*, **626**:119169, 15 May 2021. https://doi.org/10.1016/j.memsci.2021.119169

1. Introduction

With four billion people already facing water scarcity [1], water demand is only projected to intensify, fueled by a growing world population, climate change, and the rising standards of living in the developing world [2]. Tapping into nature's most abundant resource, the ocean, desalination has become a key tool for tackling the problem [3, 4, 5] with membrane-based reverse osmosis (RO) supplying the majority of the world's installed desalination capacity [2]. In spite of their success, however, membranes are plagued by fouling, often dubbed the "Achilles' heel of membrane processes", resulting in considerable downtime for cleaning and lost productivity [6].

Given the lack of effective physical cleaning methods, however, desalination plants currently rely upon chemical cleaning despite the numerous drawbacks, which include chemical costs, undesirable plant shut-downs, membrane degradation, and environmental concerns associated with chemical waste. For these reasons, alternative cleaning methods could make desalination cheaper, more widely accessible, and more environmentally sustainable.

Interest in chemical-free membrane cleaning has lately been on the rise, due to its potential to negate the drawbacks of chemical methods. Unlike other membrane processes, however, the structure of RO membranes and the module designs implemented in practice prevent direct mechanical backwashing. While the RO market had been dominated until the mid-1990's by the hollow fiber configuration, the spiral-wound configuration has lately overtaken it in prevalence due to its mechanical robustness for high pressure operation and desirable compromise among competing operating factors, such as fouling control and pressure drop [6, 7, 8]. Nonetheless, commercially existing RO membranes are unable to withstand high pressures on the permeate side during backwashing without incurring damage, nor has the piping on the permeate side in RO spiral-wound modules been designed to tolerate pressures exceeding manufacturer specifications [9].

In an attempt to provide a commercial solution combining the benefits of the spiral-wound configuration with backwashing capability, MICRODYN-NADIR recently introduced the SpiraSep 960 ultrafiltration (UF) module. The product features UF membranes that are less tightly wounded than a typical spiral-wound element, allowing for mechanical backwashing [10]. A similar product for RO, nonetheless, remains elusive. Instead, the chemical-free methods employed in RO can largely be categorized into osmotically and mechanically-driven fouling mitigation techniques.

In osmotically-induced cleaning (OIC), the net driving pressure (NDP) is controlled such that the osmotic pressure difference across the membrane becomes the dominant driving force. Water is thus transported by osmosis from the purer permeate side to the more concentrated feed side, causing the foulant layer to experience a variety of mechanisms that potentially encourage detachment [11]. Liberman and Liberman [12, 13], first coining the term Direct Osmosis cleaning by the High Salinity Solution (DO-HS), proposed such an approach as an environmentally friendly on-line cleaning technique. Further research by Qin et al. [14], Lee and Elimelech [15], and Sagiv and Semiat [16] investigated the viability of this approach for wastewater reclamation and membrane scaling mitigation.

Despite its potential, widespread adoption of OIC in practice has been challenged by operational challenges. A study by Farooque et al. [17], for example, found OIC to be ineffective at mitigating fouling in commercial spiral-wound modules used for seawater desalination. Furthermore, recent experiments by Labban et al. [11] using organic foulants demonstrate the mechanism underlying OIC and visually capture the foulant layer detachment and cleaning procedure as they occur in situ. These experiments, however, show the effectiveness of OIC decreases considerably in the presence of spacers.

Faced with these limitations for OIC, mechanically-driven vibration of the membrane presents yet another means of chemical-free fouling mitigation. While the method of generating motion can vary widely depending on the membrane configuration and geometry, the mechanism of fouling mitigation had mostly been surrounding methods that would increase the unsteady shear rate and turbulence on the membrane surface [18]. The Vibratory Shear-Enhanced Process (VSEP) is an example that employs a rotational mechanism, especially at the torsional modal frequency, to generate large oscillatory shear stresses at the membrane surface [19]. The ability of VSEP to induce large turbulent flows at the surface allows it to mitigate fouling on the membrane effectively, paving the way for treating streams featuring high fouling propensities [20]. Due to its limited capacity and high capital and maintenance costs associated with moving parts, nonetheless, VSEP may not be suitable for large-scale deployment in desalination [20, 21]. Despite the ability of rotational mechanisms to mitigate fouling, frequent chemical cleaning of the membranes remains inevitable [19]. Furthermore, higher fouling rates at smaller radii may lead to potential blockages, and uneven membrane defects.

Another mechanically-driven approach of fouling mitigation involves the introduction of hollow fiber modules, where membrane motion may be classified as longitudinal (parallel to the axis), transverse (perpendicular to the axis), or rotational. Several studies have explored the introduction of hollow fiber membrane transverse oscillation as an antifouling mechanism [22, 23, 24, 25]. In these studies, membrane vibration was achieved either by the generation of oscillating flow [25, 26] in the liquid or the direct movement of the membranes [23, 27]. Li et al. [27] performed vibration experiments with a relatively wide parameter space, concluding that transverse vibration is more effective at fouling mitigation than its longitudinal counterpart. Likewise, Kola et al. [23] estimated the energy requirements for the transverse vibration using the forces acting on the hollow fiber membranes based on empirical equations for an oscillating cylinder in a fluid, and found transverse vibration to be more efficient. However, with higher concentrations and membrane pore sizes, transverse membrane vibration was found to be ineffective as significant pore blocking may occur [23]. Additionally, the majority of the RO membranes employed commercially are in the spiral-wound configuration, rendering techniques limited to hollow fiber membrane modules less effective for current RO systems.

Other work has investigated the use of electrical signals [28, 29], magnetic field [30], or more recently the motion of spacers [31, 32] to mitigate fouling. Studies featuring direct membrane motion demonstrate that fouling mitigation is enhanced by operating at conditions that increase the shear rate at the membrane surface

[33]. Existing studies, however, have either focused on configurations not viable in large-scale desalination [21], or explored only a bench-scale approach with no consideration for large-scale deployment on existing RO systems [33, 34]. While a vibratory method coupled with the understanding that a resonant frequency of the structure enhances antifouling is not a new concept, the prediction of a natural modal frequency is necessary and can be problematic. Consequently, the universal challenge of membrane fouling, compounded by the lack of effective chemical-free cleaning technology that is applicable to commercial systems, underscores the pressing need for an alternative.

2. Motivation and research objective

The spiral-wound module (SWM) has become the most common configuration for commercial RO systems by successfully balancing the requirements of surface-area-to-volume ratio, pressure drop, fouling control, and ease of operation [7]. A typical desalination plant, for example, features hundreds to thousands of such modules depending on its capacity and feed water salinity [6]. The SWM configuration, depicted in Figure 1A, is primarily composed of the feed and permeate flow channels, spacers, permeate tube, and pressure vessel. Membranes leaves, connected to a central permeate tube, are rolled into a spiral. Individual leaves are separated by feed spacers that encourage mixing and deter fouling.

The complicated geometry involved can make the development and implementation of an effective physical cleaning method particularly challenging. Despite this complexity, however, a portion of the SWM configuration may be approximated as a flat-sheet, as shown in Figure 1A, provided that $\delta x/d \ll 1$, where δx represents the membrane thickness and d is the diameter of the corresponding section. Accordingly, a bench-scale flat-sheet module is first adopted as a model coupon herein to examine the cleaning in situ before experiments are run on a commercial SWM.

Figures 1B and 1C demonstrate the method proposed in this work and how it fares relative to traditional chemical cleaning. Instead of introducing harsh chemicals such as HCl or NaOH, biocides, or oxidants, deformation-induced cleaning (DIC) relies on controlled mechanical deformation, as shown in Figure 1B. The DIC procedure is chemical-free, reducing overall waste production while simultaneously eliminating the purified water consumption otherwise necessary to prepare the cleaning solution [6]. In addition, DIC is expected to be cheaper, drastically lowering system downtime associated with cleaning, as illustrated in Figure 1C and demonstrated later in this study.

Compared to other chemical-free alternatives, DIC introduces several elements of novelty in RO fouling mitigation. Unlike traditional mechanical backwashing that relies on reversing the flow across a membrane, DIC derives its effectiveness from shear stresses, induced at the membrane-foulant interface, that result in foulant detachment and membrane cleaning. The distinction is important as the proposed approach lowers the risk of delamination or damaging the ultra-thin selective layer in RO when deformation is properly controlled and may enable continuous RO operation with fouling control. As shown later in this work, this distinction is even more relevant when coupled with mechanical fatigue of the membrane-foulant interface

induced by cycling to deliver effective fouling mitigation at lower deformation amplitudes that ultimately preserve the membrane integrity. To the best of the authors' knowledge, this study in fact presents the first attempt to employ mechanical fatigue in enhancing chemical-free fouling mitigation.

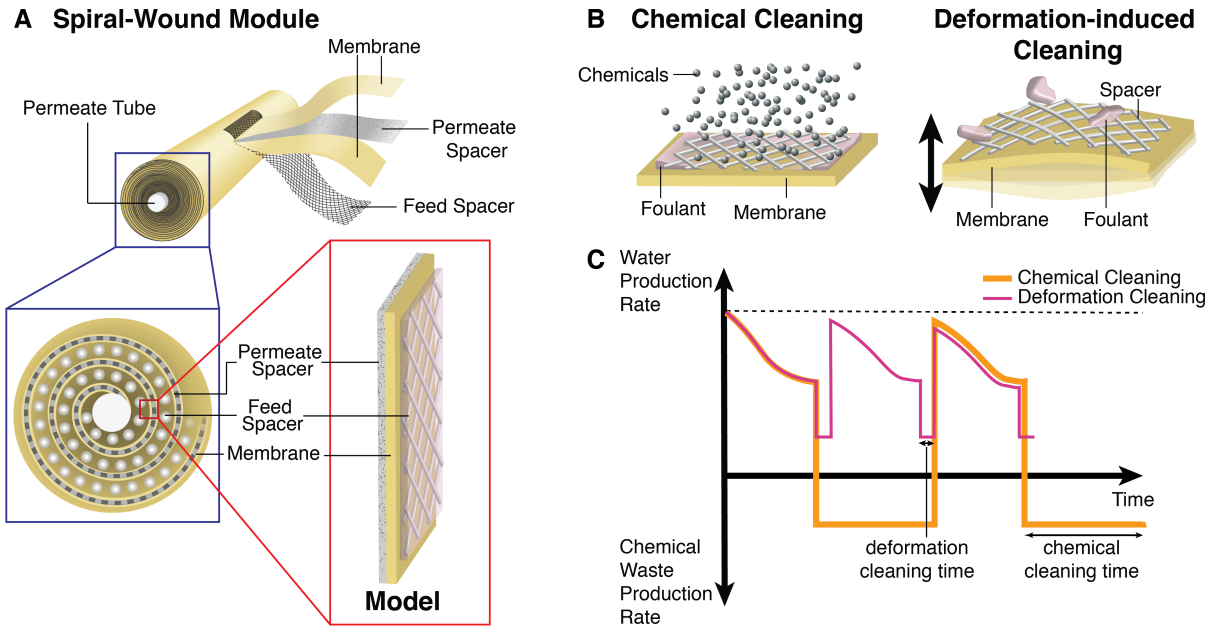

Figure 1. Potential of deformation-induced cleaning: A) Illustration of the spiral-wound module and structure. The model coupon emulates the hydrodynamics of one section of the spiral-wound module. B) Comparison of the mechanics of conventional chemical cleaning and the deformation-induced cleaning procedure proposed herein. C) A comparison of the two methods in terms of water production/chemical waste generation and their respective cleaning times (figure not drawn to scale).

While induced hydrodynamic stresses are often responsible for foulant removal in other chemical-free alternatives, fouling mitigation in DIC is attributed to mechanical stresses that target and weaken the membrane-foulant interface directly. The result is more effective fouling mitigation at a lower cost given that deforming a thin surface incurs a considerably lower energy penalty than mechanically vibrating the entirety of the flow system as in other technologies such as VSEP. Although DIC is promising, its large-scale implementation and long-term effectiveness remain open questions.

In this work, we address the need for effective chemical-free membrane cleaning by proposing DIC as a new RO cleaning method potentially applicable to the SWM. Experiments involving brackish feed water and organic fouling using alginate are first run on a bench-scale flat-sheet module. Having the scientific findings of the flat-sheet studies, DIC is then attempted on a commercially available SWM. Despite cleaning durations being six-fold lower for DIC, the results demonstrate cleaning efficiencies comparable to chemical methods and indicate applicability to commercially available modules. By using experimental setups designed for in situ visualization, this work seeks to provide insights into the cleaning procedure based on fundamental principles. For the first time we establish a direct relationship between membrane deformation, interfacial

shear strength, and surface cleaning for membrane applications. Fatigue of the interface (see Section 4.2) is shown to be responsible for the cleaning observed. We end this work by introducing a case study providing an economic assessment of the potential of DIC. Our results suggest the cleaning method proposed can considerably lower the costs of desalination plant operation while increasing average fluxes and reducing specific energy consumption.

3. Materials and methods

3.1. Cross-flow experiments

3.1.1. Flat-sheet module

The flat-sheet module was selected to allow for in situ visualization of the membrane deformations and the subsequent cleaning of the organic foulant layer. The setup, as designed by Tow et al. [35] and illustrated in Figure 2, consists of a thin-film polyamide-polysulfone composite reverse osmosis (RO) membrane, with dimensions of 0.08 m by 0.03 m, housed in a plate-and-frame module, capable of withstanding pressures of up to 69 bars (gauge). The custom built module was fashioned out of 316 stainless steel for its high mechanical strength and corrosion resistance. To allow for viewing in situ, a 0.04 m by 0.03 m window was carved out and replaced with polycarbonate.

The polycarbonate was installed, and subsequently polished, so that it sat flush with the stainless steel to prevent flow disturbance. Manifolds were milled on the feed channel to mitigate entrance and exit losses in the flow. The feed and permeate channels were designed to be 0.08 m long and 0.03 m wide, as per the membrane area, and with 0.55 cm depth to simulate the flow in the feed channel of a spiral-wound RO module. A 28-mil feed spacer from a commercial spiral-wound module (Dow TW30-2514) was placed in the feed channel to simulate actual flow conditions. Five permeate spacers, with a total thickness of 1 mm, were placed in the permeate channel to support the membrane during RO filtration.

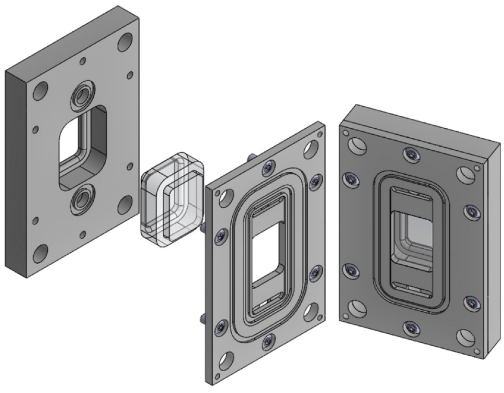

Figure 2. Flat-sheet module[1]: Filtration cell adopted during cross-flow experiments. The cell, designed for in situ visualization, consists of a feed and a permeate side with an exposed membrane area of dimensions 0.08 m × 0.03 m and a visualization window of dimensions 0.04 m × 0.03 m.

3.1.2. Spiral-wound module

In order to demonstrate the applicability of deformation-induced cleaning (DIC) to the spiral-wound configuration, a commercial RO module (Dow TW30-2514) intended for brackish water, was adapted. The spiral-wound element has a reported active area of 0.7 m^2, featuring a polyamide-polysulfone thin film composite membrane. A 28-mil feed spacer is incorporated in the module to separate adjacent active layers and prevent physical contact. Furthermore, a complementary metallic housing and end caps were selected, enabling RO filtration at high pressures of up to 15 bars. To allow for visualization of membrane deformations in the module, a transparent cylinder was machined out of polycarbonate, mimicking the exact dimensions of the metallic housing.

3.1.3. Cross-flow apparatus

The cross-flow within the membrane modules was maintained using positive displacement pumps (Hydra-Cell F20 and Hydra-Cell D10), controlled by a variable frequency drive (VFD). To alleviate the pulsing effects caused by the positive displacement mechanism, pulsation dampeners (Hydra-Cell 4CI SST) were installed in the feed stream of both setups. Positioned along the feed and permeate flow streams of both setups were pressure transducers with 1% accuracy of the reading (Wika A-10), whose digital outputs were converted via a data acquisition module (DAQ) and monitored in real-time using the LabView software. The permeate flow rates were recorded using a digital mass scale with 0.01 g readability (Carolina SLB302) and a digital flowmeter with 1% accuracy of the reading (McMillan S111-5) for the flat-sheet and spiral-wound modules respectively. For experiments conducted on the flat-sheet module, a moving average of 5 minutes was adopted to report values of the permeate flux based on readings collected from the mass scale. Back-pressure regulators were employed to adjust the feed pressure while flowmeters on the feed and permeate streams recorded the corresponding volumetric flow rates. In accordance with values encountered in practice, the cross-flow velocity was set at 0.085 m/s, and the initial flux was maintained at 25 LMH with a feed pressure of $\sim$15 bars for all fouling experiments.

[1]Reprinted from *Desalination*, 399, Tow et al., In situ visualization of organic fouling and cleaning mechanisms in reverse osmosis and forward osmosis, 138–147, Copyright (2016), with permission from Elsevier.

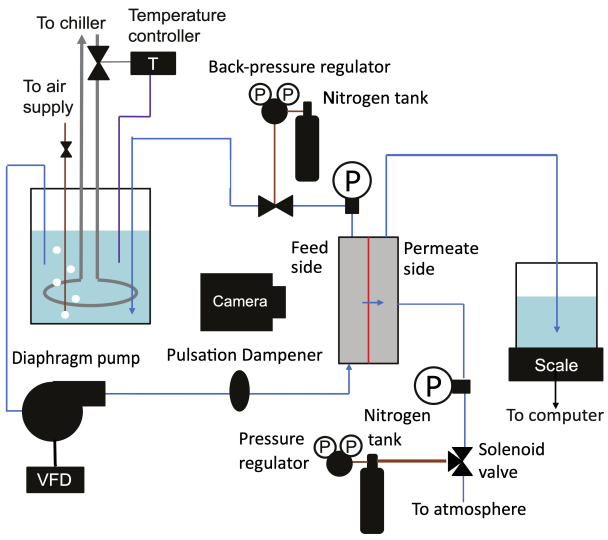

Figure 3. Schematic diagram of the cross-flow filtration apparatus: Feed water is introduced into the flow system via a positive displacement pump, controlled by a VFD. Transducers record system pressure maintained by a back-pressure regulator or a solenoid valve connected to pressurized nitrogen or inert air. Temperature was set via a controller connected to a chiller. A camera was employed for in situ visualization, while a bubbler was introduced to ensure proper mixing of the feed.

3.1.4. Feed solution and chemicals

In this work, the feed and cleaning solutions were prepared using commercially available stock chemicals from Sigma-Aldrich and Alfa Aesar. To generate a 10 g/kg (0.28 M) NaCl solution, the estimated NaCl concentration of brackish water, 80 g of anhydrous NaCl was added to 8 kg of deionized water. Conductivity measurements of the feed and permeate solutions were recorded using a conductivity meter with 1% accuracy of the reading (Ultrameter III, Myron L Company, Canada). A gas bubbler was used to generate turbulence for mixing and salt dissolution, and a temperature control feedback loop was employed to maintain the solution temperature at 20° C.

For fouling experiments, sodium alginate (Sigma-Aldrich A2033) was used as the model organic foulant and was introduced into the feed at a net concentration of 0.25, 0.5 and 1.0 g/kg. Alginate, with molecular weights ranging from 80,000 to 120,000 g/mol, is an extensively-studied and widely adopted model organic foulant for its gel-forming properties and resemblance to extracellular polymeric substances (EPS) encountered in fouling and found in municipal wastewater and commercial desalination [35, 36, 37, 38]. Thereafter, $CaCl_2$ (Alfa-Aesar) was added at concentrations of 1.25, 2.5, and 5.0 mM corresponding to the different alginate concentrations to initiate complexation with the alginate polysaccharide and produce the organic foulant film on the membrane during filtration.

To improve foulant visibility during cleaning experiments, methylene blue (1% by weight) was occasionally added to stain the polymerized alginate layer, allowing for the elucidation of the cleaning mechanism. Methylene blue (Sigma-Aldrich) was chosen as previous studies had demonstrated minimal effect on fouling

characteristics under low salinity feed (lower than 20,000 ppm) [35]. In this work, experiments featuring methylene blue were run independently from other experiments used for data collection, and the results were only used for in situ visualization and qualitative assessment of cleaning performance. Following preparation, the feed solution was finally introduced into the corresponding cross-flow system (flat-sheet or spiral-wound), pre-washed with deionized water. Due to the water in the system, the final concentrations were effectively diluted by an estimated 0.4 L for the flat-sheet module, and 1 L for the spiral-wound module. The final concentrations are summarized in Tables 1–2 for ease of reference.

Table 1. Final concentrations adopted for the flat-sheet cross-flow filtration experiments.

Feed constituent	Final Concentration
NaCl (g/kg)	9.5
Alginate (g/kg)	0.95
$CaCl_2$ (mM)	4.76
Methylene blue (µM)	7.23

Table 2. Final concentrations adopted for the spiral-wound cross-flow filtration experiments.

Feed constituent	Case 1	Case 2	Case 3
NaCl (g/kg)	8.9	8.9	8.9
Alginate (g/kg)	0.88	0.44	0.22
$CaCl_2$ (mM)	4.44	2.22	1.11

3.1.5. Deformation-induced cleaning (DIC) protocol

Deformation-induced cleaning on the RO membranes was performed once the normalized flux readings fell to the threshold value. The flux measurement instruments were then paused, the static pressure of the feed stream was gradually reduced to 2.0 bar using the back-pressure regulator, and the cross-flow velocity was adjusted through the VFD to 0.25 m/s (Figure 3). This velocity was adopted to match that of the high speed circulation phase of the chemical cleaning protocol as outlined in Section 3.1.6.

Thereafter, the permeate-side channels were connected to a three-port solenoid valve (SMC VQZ115-5M-C4-PRF), with the main port exposed to the atmosphere while the secondary port was connected to a pressurized air stream of 2.25 bars from a secondary inert air supply. Membrane deformations were induced through periodic pressurization and depressurization of the permeate channel through the solenoid valve, where the frequency and duration of oscillations were preprogrammed and controlled by an external micro-controller setup. The frequency and cleaning duration were set at 0.5 Hz (one complete deformation cycle every 2 s) and 15 mins. This frequency was selected through experimentation by balancing considerations such as pneumatic valve limitations, cleaning efficacy, and preserving membrane integrity. The cleaning

duration was selected based on the time recommended by the membrane manufacturer for recirculating the cleaning solutions (details in Section 3.1.6). After cleaning, the solenoid valve assembly was subsequently disconnected, and the scale was reattached to the permeate-side channel for post-cleaning flux measurements.

3.1.6. Chemical cleaning protocol

To enable comparisons with chemical cleaning, the EDTA/Na_4EDTA acidic buffer solution, as recommended by Dow's chemical cleaning protocol [39], was prepared by dissolving EDTA (Sigma Aldrich) pellets in an NaOH aqueous solution at 4:1 molar ratio. Furthermore, as stipulated, additional NaOH was added drop-wise into the resultant solution to raise the pH to 12 before the solution was cycled into the module for chemical cleaning. The procedure of chemical cleaning is as follows: 1) The feed solution in the system was completely displaced by the cleaning solution, as indicated by the pH of the resulting reject stream; 2) once the system was filled with cleaning solution, the solution was recirculated in the module at 0.125 m/s for 15 mins; 3) the module was then left to soak for at least an hour. 4) The cleaning solution was recirculated in the system on high speed for 30 – 60 mins. The cross-flow velocity employed, similar to DIC, was set at 0.25 m/s. 5) The cleaning solution was then completely flushed out by deionized water recirculated for another 30 mins, before the feed water was introduced again to continue with the filtration operation.

3.1.7. Key performance metrics

Three metrics, flux recovery, cleaning efficiency, and salt rejection, were monitored when assessing the effectiveness of DIC at foulant removal. Flux recovery quantifies effectiveness by measuring the difference in normalized flux before and after cleaning with respect to the initial flux. In contrast, the cleaning efficiency, defined in Equation 1, accounts for the severity of fouling by considering how flux recovery compares to the maximum recoverable flux:

$$\eta = \frac{\bar{J}_{cleaned} - \bar{J}_{fouled}}{1 - \bar{J}_{fouled}} \tag{1}$$

In Eq. 1, $\bar{J}$ refers to the recorded flux normalized with respect to the initially recorded flux for a pristine membrane. Salt rejection is defined as the percentage of dissolved salts rejected by comparing permeate and feed salt concentrations:

$$R = 1 - c_p/c_f. \tag{2}$$

This metric provides a direct measure of membrane integrity: a sudden decrease in rejection (or increase in permeate concentration) signals potential membrane damage, typically in the form of tears or defects in the membrane's active layer.

3.2. No-flow experiments

In analyzing the foulant-membrane interactions, the attraction between the alginate and the membrane can be described in terms of the presence of physical bonds between the two. The physical bonds include van

der Waals and electrostatic interactions, collectively described by the Derjaguin-Landau-Verwey-Overbeek (DLVO) theory, hydrogen bonds, and hydrophilic interactions [40, 41]. Previous research on rotating membranes and on vibrating hollow fiber membranes demonstrated that inducing shear stresses at the membrane surface could mitigate fouling [20, 18, 23, 27]. However, it is important to distinguish between the effects of shear stresses induced by membrane deformation from those induced by cross-flow when evaluating the performance of DIC. Accordingly, this section focuses on no-flow experiments featuring only membrane deformation in the absence of both cross-flow and high applied pressure.

In these experiments, the relevant parameter to characterize the foulant-membrane interaction is the interfacial shear stress generated by the deformation of the membrane. The thickness of the membrane-alginate bilayer is significantly smaller than the other dimensions, so the stresses developed in the materials and at the interface can be estimated using the Kirchhoff-Love plate theory [42] based on an assumed deformed shape. The shear stress profile, and consequently the interfacial shear stress, can then be evaluated through the equilibrium of the in-plane stresses within each of the individual layers. Detailed derivations and approximations can be found in Appendix A. While the stress derivations determine the level of driving force to break the physical bonds between the membrane and the foulant, the impact of interfacial fatigue or damage still needs to be quantified experimentally. Thus, the experiments presented next were designed to study the impact of the interfacial stresses generated on the shear strength of the membrane-foulant interface.

3.2.1. Specimen preparation

Dow TW30-2514 membranes were cut into coupons having a size of approximately 0.11 m by 0.06 m. A stencil was placed on the membrane such that only a 0.08 m by 0.03 m section is exposed, and a sodium alginate solution (2% by weight) was spread on the exposed section. The membrane was then spin-coated at 250 rpm to obtain a uniform layer of the solution, and soaked in a calcium chloride solution (1% by weight). The ratio of the concentration of sodium alginate and calcium chloride is maintained at approximately 2:1 by weight to match the main experiments. A concentration of 2% sodium alginate was selected as it is sufficiently viscous to generate a contiguous and uniform layer. A thin uniform film of alginate of 400 μm was formed using this process. Furthermore, the process presented herein was selected, as it produces alginate gel of constant thickness and stiffness within five minutes, such that a parametric study on the effect of deformation on the interface can be conducted.

3.2.2. Deformation experiments

Fig. 4 illustrates the experimental setup for the deformation experiment. The contaminated membrane was then placed in a cell module, which was designed to be a simplified version of the module described in Section 3.1.1. O-rings sat inside milled grooves on each side of the module halves such that when the module was closed, the membrane is held in place and seals for two separate channels were created. Each half of the module has two inlet/outlet ports, through which the channels are filled with deionized water during the

deformation experiments.

On the support side of the membrane, each inlet/outlet port was connected to a 20 mL syringe, where the displaced volume was controlled by syringe pumps. On the other side, one of the ports was sealed while the other was connected to a half-filled 20 mL syringe to enable variable volume in the channel, as the membrane is deformed. Care was taken to ensure that bubbles and air pockets were removed prior to deformation. During the deformation experiments, the two syringe pumps were controlled to dispense (and withdraw) water into (and from) the channel at a rate of 18 mL/min for 5 s or 3 mL in total. Assuming the mode shape presented later in Appendix A.1, the volume per unit deflection was estimated through integration. Based on the amount of water dispensed, the maximum deflection was estimated to be ~ 0.5 mm. The syringe pumps were controlled to dispense and withdraw for the desired number of cycles before being removed from the model cell for interfacial shear strength measurement. In this study, 0 to 50 cycles, at intervals of 10 s, were applied. This is because the interface between a pristine membrane and the foulant has weakened sufficiently to separate by itself beyond 60 cycles.

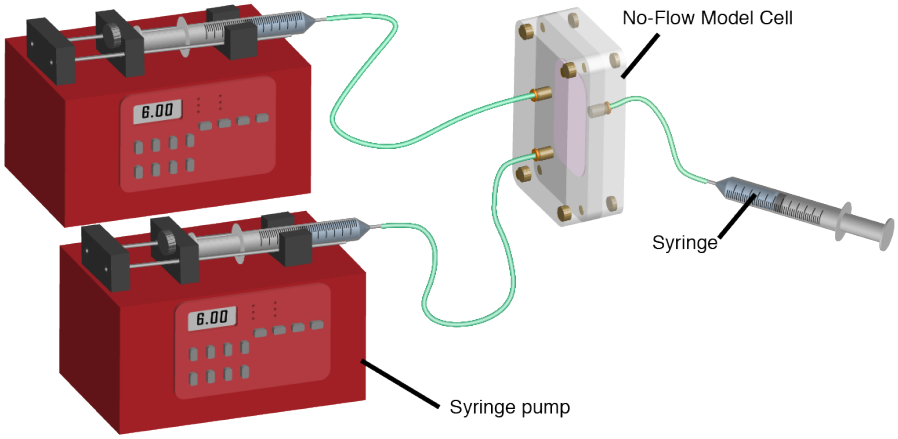

Figure 4. No-flow deformation experimental setup: The membrane is placed in the no-flow model cell, which creates two separate volumes. Syringes are mounted on the syringe pumps and the volume on the left side of the no-flow model cell is controlled by their displacement. The syringe on the right side of the cell allows the volume on the right side to be variable, as the membrane deforms.

3.2.3. Lap shear experiments

A thin piece of polyester (PET) shim stock (50% longer than the alginate film) was glued carefully to the alginate film using a thin layer of cyanoacrylate. The loose part of the PET shim was attached to the vertical component of the universal testing machine (Zwick BTC-FR2.5TH.D09), and the membrane-alginate-PET specimen was secured to the table fixture. The machine was loaded with a 20 N load cell with a precision of 4 mN and was controlled to pull apart at a rate of 20 mm/min, and the maximum force was recorded. (This test was performed in a similar manner to ASTM D3163.) The section where the alginate is attached to the membrane is a rectangular area of length 0.08 m and width 0.03 m. The

shear strength of the interfacial layer is thus the force required to shear the area divided by the area of the adhered section, or 0.0024 m^2. The shear stresses measured using this method should be higher than if the gel were formed under dynamic filtration, as the alginate concentration is higher in these no-flow experiments, contributing to greater interfacial interactions. Furthermore, for a foulant gel formed under dynamic filtration, the interaction is likely to be weakened due to the presence of hydrophilic interactions. Nevertheless, the stress values obtained in these experiments could still inform the trend of the overall effect of deformation and shear strength under dynamic filtration.

After the lap shear experiments were conducted, a membrane sample was rinsed gently and the same experiment was repeated for the same number of deformation cycles until the membrane has been fouled and cleaned a total of five times to investigate the effect of irreversible fouling.

3.2.4. Adhesion Energy Measurement

Instead of securing the membrane to the table fixture, the membrane was secured on a horizontal linear stage. The horizontal stage was designed to move the same distance as the vertical motion, keeping the angle between the strip and the membrane the same. The initial adhesion energy was found by measuring the force required to peel the strip and alginate from the membrane at quasi-steady conditions ($\sim$ 5 mm/min). The force, F [N], and adhesion energy, Γ [J/m^2], were then related by $\Gamma = \frac{F}{a}$, where a is the width of the alginate film.

4. Results and discussion

Experiments were conducted on both small-scale flat sheets of membranes and on a commercially used spiral-wound membrane module (SWM).

4.1. Flat sheet module

Figure 5A illustrates the difference between regular filtration operation and cleaning operation of the module. During regular filtration, the permeate flows through the membrane into the permeate tank, where the flux is recorded. As the membrane fouls, the permeate flux reduces to a pre-defined threshold, in this case 65%, at which point DIC is initiated. Fouling rates have been accelerated herein to investigate the cleaning repeatability across multiple cycles of fouling and cleaning.

During DIC operation, the pressure on the feed side is reduced to ~ 2 bar, while pressure on the permeate side is modulated through a dedicated solenoid valve connected to the permeate channel. A square wave voltage of 0 to 5 V drove the valve, resulting in a permeate gauge pressure variation of 0 to 2.25 bar around a baseline pressure of 0 bar, leading to membrane deformation. Specifically, the alternating sign of the net applied pressure causes the membrane to deflect toward and away from the feed spacer, generating dynamic stresses in the foulant film and the membrane. In this process, the pressure is controlled so that the net applied pressure on the membrane's permeate side does not exceed 0.3 bar, following the recommendation of the membrane manufacturer.

Figure 5B shows the results for three fouling and cleaning cycles conducted on the flat-sheet module. DIC achieves cleaning efficiencies of 35–46% with flux recoveries between 13–17%, while maintaining a salt rejection above 95%. The pattern of diminishing returns observed with flux recovery and cleaning efficiency is expected and is a characteristic of irreversible fouling typically experienced by membrane systems. These results are comparable to chemical cleaning (Figure 5D) and demonstrate the great potential of DIC for chemical-free cleaning.

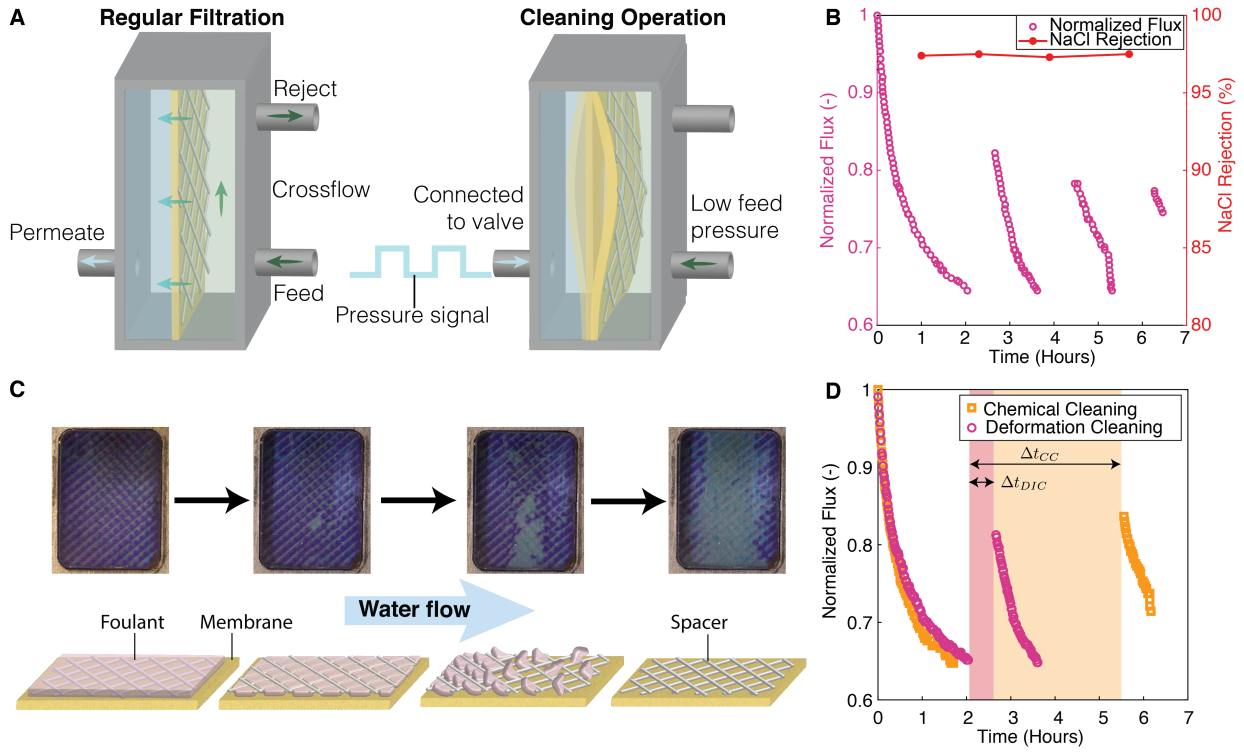

Figure 5. Demonstration of deformation-induced cleaning: A) Illustration of regular filtration and cleaning operation modes. During the cleaning operation, a permeate pressure signal is introduced, causing the membrane to deflect. B) Plot depicting the normalized permeate flux as a function of time for the flat-sheet module. After fouling, three DIC cycles were introduced, demonstrating the repeatability of flux recovery. C) Video stills and a corresponding illustration capturing the mechanics underlying DIC. The alginate layer was cut into smaller pieces by the relative motion between the membrane-alginate layer and the feed spacer. The alginate pieces then easily delaminate and are carried away by the flow. The original video is contained in the Supplementary Information. D) Comparison of DIC to chemical cleaning, whose corresponding durations are denoted by Δt_{DIC} and Δt_{CC}. Included in both is an additional 15 mins of run-time necessary to obtain a flux measurement.

To visualize the cleaning mechanism, a separate experiment was conducted on the flat-sheet module with methylene blue dye added to the feed, staining the alginate gel [35]. Video stills, captured from an in situ recording of DIC, are shown in Figure 5C. As a result of the relative motion between the membrane-alginate layer and the feed spacer, the alginate film is effectively cut into small pieces within the first few cycles, as the figure depicts. Subsequent cycles then resulted in the delamination of the pieces near the center of the coupon before propagating to the sides. As the film is cut into smaller sections, each section must individually overcome the adhesive forces between itself and the membrane, and at the same time the stresses experienced by the individual pieces varies depending on their location (further discussion in Appendix A.2.2). After 15 minutes of DIC, some alginate pieces on the edges are still visibly attached, explaining the imperfect cleaning observed in Figure 5B.

Furthermore, the efficacy of DIC relative to state-of-the-art chemical cleaning was evaluated by running cleaning experiments using a solution of Tri-Sodium Ethylenediaminetetraacetic acid (EDTA) in a sodium

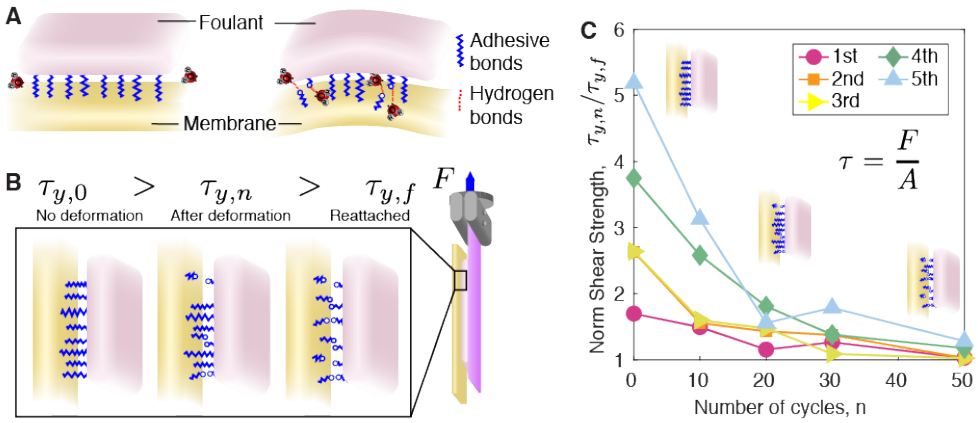

Figure 6. Mechanics of deformation-induced cleaning: A) Illustration of the physical bonds between the alginate and membrane in its original state and after some deformation. B) Illustration of the measurement of shear stresses between the alginate and membrane. With more physical bonds broken, the shear stresses are expected to reduce. C) Normalized shear stresses after n deformation cycles in addition to the number of times the membrane has been fouled.

hydroxide pH buffer. The procedure is in accordance with the protocol recommended by the manufacturer [39], whose details are provided in Section 3.1.6 for reference. Experimental results, comparing the results from DIC to chemical cleaning of the flat-sheet module, are summarized in Figure 5D. While both methods demonstrated relatively similar flux recoveries (17% and 20%) and cleaning efficiencies (46% and 53%), the duration for chemical cleaning, Δt_{CC}, is six-fold longer than that of DIC, placing chemical cleaning at a considerable disadvantage. The slightly higher recovery attained by chemical cleaning, however, may be attributed to the ability of the cleaning solution to reach membrane edges used for support, where interfacial stresses remained low during DIC.

4.2. Foulant-membrane interactions and underlying mechanisms

To quantify the effect of deformation alone on the alginate-membrane adhesion, no-flow deformation experiments were conducted to measure the force required to shear the alginate layer off of the membrane as discussed in Section 3.2. The maximum cyclic deformation of the membrane, estimated based on the volume of water pumped into the cell, is ± 0.5 mm. Maximum cyclic interfacial shear stresses of approximately ± 10 Pa were generated. As noted previously, the shear stresses arising here are attributed to structural equilibrium necessary for the deformation of the membrane-foulant bilayer, and it is important not to conflate this stress with that of shear stresses arising due to hydrodynamics.

The lap shear tests were conducted in air to provide a better characterization of the alginate-membrane interfacial strength before and after deformation, and changes in its frictional properties. When tests are performed in aqueous conditions, the detached interface between the alginate and the membrane will be lubricated by water, resulting in low frictional forces. Thus, the shear forces measured in an aqueous condition are not indicative of the effect of membrane variability on the effective alginate-membrane interfacial strength.

The reversible shear strength due to friction, $\tau_{y,f}$ — the shear strength of the reattached alginate and membrane interface in air, in the range of 40-100 Pa — of each samples were used to normalize the measured shear strength of the alginate-membrane interface as presented in Figure 6C.

As depicted in Figure 6B, an undisturbed interface has a higher shear strength, $\tau_{y,0}$, compared to the shear strength after n number of cyclic deformations, $\tau_{y,n}$. The measured normalized shear strength of the interface decreased drastically with the number of cycles (Figure 6C), approaching the reversible shear strength within 50 cycles. With repeated fouling, the shear strength prior to cyclic deformation increased, an indication of increased difficulty of mechanical cleaning with repeated fouling. Nevertheless, the results suggest that the number deformation cycles may need to be increased for repeatedly fouled membranes, while at the same time suggest that only a very low number of cycles is needed for fresh membranes. The weakening of the material properties, in this case the interfacial shear strength, is a phenomenon known as fatigue, which is described as the partial breakage of some of the physical adhesive bonds [43, 44, 45] (Figure 6A). Fatigue is also mathematically represented as an exponential or power law decay from τ_0, the initial shear strength, to τ_∞, the asymptotic shear strength [43], a trend consistent with the observations represented in Figure 6C. This trend suggests that the interfacial shear stresses of $\pm$ 10 Pa generated by the deformation of the bilayer have already exceeded the fatigue threshold of the interface, i.e. that these stresses are sufficient to induce bond breakage at the interface.

Eventually, cyclic deformation will result in sufficient damage to the interface that delamination of the foulant occurs. There are two possible mechanisms of foulant delamination: shear stress – when the interfacial shear stress exceeds the shear strength – or strain energy release rate – when the per unit area strain energy stored in the film exceeds the adhesion energy. The mechanism by which the foulant delaminates can be characterized by the ratio of the length of the bonded alginate foulant along the membrane surface and a critical length scale defined by $L_c = \frac{k}{2(1+\nu)}\sqrt{2E_a\Gamma h_a/{\tau_y}^2}$, where k is a non-dimensional prefactor based on the cross-sectional properties, while E_a, ν, and h_a are the Young's modulus, Poisson's ratio, and the thickness of the alginate layer respectively, and Γ is the energy per unit area required to separate the alginate from the membrane. This critical length scale was evaluated by equating the required applied deformation for failure due to shear and strain energy release rate, a result derived in Appendix A. Golovin et al. [46] described a similar critical length of the bonded section, $L_c = \sqrt{2E_a\Gamma h_a/{\tau_y}^2}$, which was derived by assuming a maximum applied force in a direction parallel to the membrane.

If the bonded length, or the length of the alginate section that is attached to the membrane, is lower than L_c, the interface fails when the interfacial shear stress exceeds the shear strength. In contrast, if the bonded length is higher than L_c, the interface fails when the per unit area strain energy stored in the film exceeds the adhesion energy. Based on an order of magnitude estimate, the critical length scale herein is $L_c \sim O(20)$ cm, which is larger than the dimensions of the membrane. Earlier visualization of DIC also showed the alginate layer being cut by the feed spacer into smaller pieces with a bonded length of the same size as the feed spacer grid of 2 mm. Since this bonded length is lower than the estimated critical length

scale, the sections can be assumed to delaminate once the interfacial shear stresses exceed the instantaneous shear strength. As the interfacial shear stresses are zero at the edges of the membrane, those alginate pieces remained attached, consistent with the results observed in Figure 5C.

4.3. Spiral-wound module

Despite the success demonstrated on the flat-sheet module, tighter spacing constraints encountered in the SWM may restrain maximum membrane deformation, reducing DIC efficiency in practical configurations. Additionally, tighter spacing might bring the membrane and spacer in the SWM closer together during DIC, posing an increased risk of membrane damage. Accordingly, experiments were conducted on a commercially-available spiral-wound RO module (Filmtech TW30-2514) to assess DIC's applicability to realistic configurations.

The experimental setup employed is shown in Figure 7A. While a stainless steel vessel was used in actual filtration and cleaning experiments on the SWM, a transparent vessel was adopted when conducting visualization experiments. An artificial waterline, shown in Figure 7A, was set on the transparent vessel to assist in visualization. As the permeate side is pressurized during DIC, the water level in the vessel rises, indicating membrane deformation associated with a slight expansion of the SWM. In contrast, the drop in the water level indicates a reversal in SWM expansion in response to depressurization. Together, this cycle of pressurization and depressurization induces a deformation response in the SWM membranes that can be exploited for cleaning.

Three sets of experiments, featuring different alginate concentrations (1 g/kg, 0.5 g/kg, and 0.25 g/kg), were conducted to evaluate the effectiveness of DIC against varying degrees of fouling on the SWM. Varying the foulant concentration brings about films of various consistencies and mechanical properties, providing a more representative assessment of DIC applicability across different fouling conditions. Fouling and cleaning experiments conducted on the SWM are summarized in Figures 7B–D.

As expected, fouling severity increases with the concentration. Flux recovery shows a pattern of diminishing returns, indicative of irreversible membrane fouling. For the first cleaning cycle, the highest cleaning efficiency is observed with the lowest foulant concentration (0.25 g/kg), at a high of 82%. However, irreversible fouling quickly sets in as the cleaning efficiency for feed water with the lowest concentration reduced drastically over the next two cycles as compared to the high concentration (1 g/kg). Furthermore, the best cleaning performance was recorded with a 0.5 g/kg foulant concentration, achieving cleaning efficiencies ranging between 33–78% over three cleaning cycles. More importantly, however, the notable flux recovery recorded across all concentrations, while membrane salt rejection is consistently preserved, demonstrates that DIC may be adaptable to commercial SWM's.

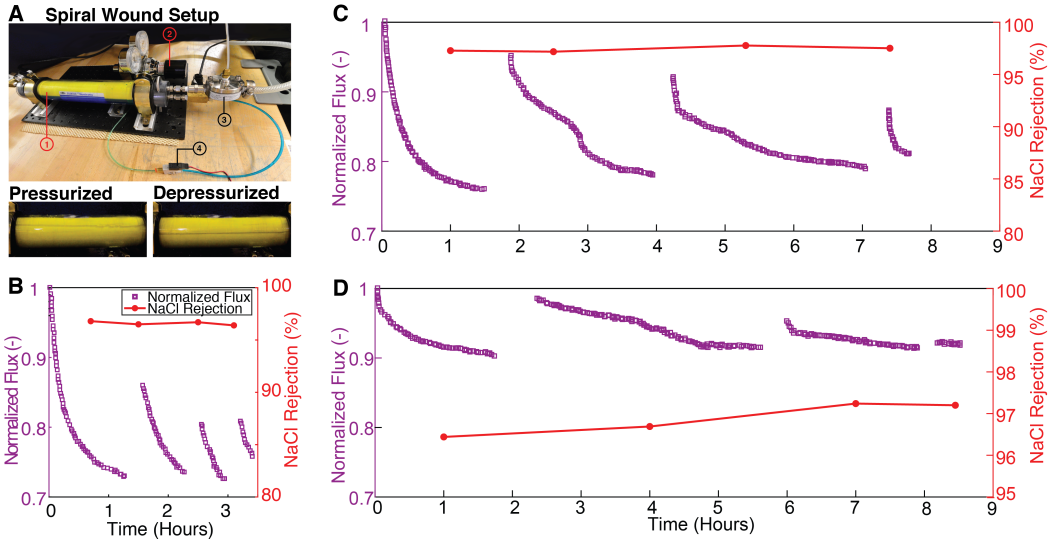

Figure 7. Spiral-wound module experiments: A) In this bench-scale module, a transparent polycarbonate vessel is adopted for in situ visualization. A three-port solenoid valve is employed in controlling the permeate-side pressure during DIC. A back-pressure regulator is used in setting the feed-side operating pressure, while a pressure regulator delivers the necessary pressure to the three-port valve for DIC operation. B–D) Plots of normalized permeate flux and salt rejection for different alginate concentrations (1 g/kg, 0.5 g/kg, and 0.25 g/kg). Three DIC cycles are applied, demonstrating applicability across a spectrum of fouling propensities. Steady salt rejection indicates membrane integrity is preserved during DIC.

5. Implications

The previous sections demonstrated the implementation of DIC, its performance compared to chemical cleaning, and its effectiveness on the SWM. To evaluate its implications for desalination plant operation, however, a case study, comparing the performance of DIC to chemical cleaning for a model 24,000 m^3/day brackish water plant, is presented. Plant specifications, selected following industry standards [6, 47, 48, 49], are summarized in Appendix B together with relevant derivations and modeling assumptions.

To capture the effect of fouling propensity on technology effectiveness and adoption, two cases, featuring low (Figure 8A) and high (Figure 8B) degrees of fouling are considered. These figures show the plant's average flux, specific energy consumption, and cost of cleaning as functions of the time between cleanings, Δt_c. In these figures, typical chemical cleaning operation for each case is denoted by a circle, while optimal DIC operation is denoted by a square. In practice, the frequency of membrane cleaning depends on the feed quality and pretreatment provided, and should be controlled for optimal plant operation.

In Figures 8A–B, the maximum and minimum (denoted by blue lines herein) represent the plant's maximum average flux and minimum specific energy consumption possible under the ideal limit of no fouling. In this limit, the desalination plant experiences no flux decline due to fouling, and correspondingly no cleaning shutdowns. The shaded regions, however, highlight the plant's actual deviation from this limit for a specified Δt_c. As shown in the figures, such deviations may be attributed primarily to fouling (in the limit of high

Δt_c) or excessive plant shutdowns (in the limit of low Δt_c).

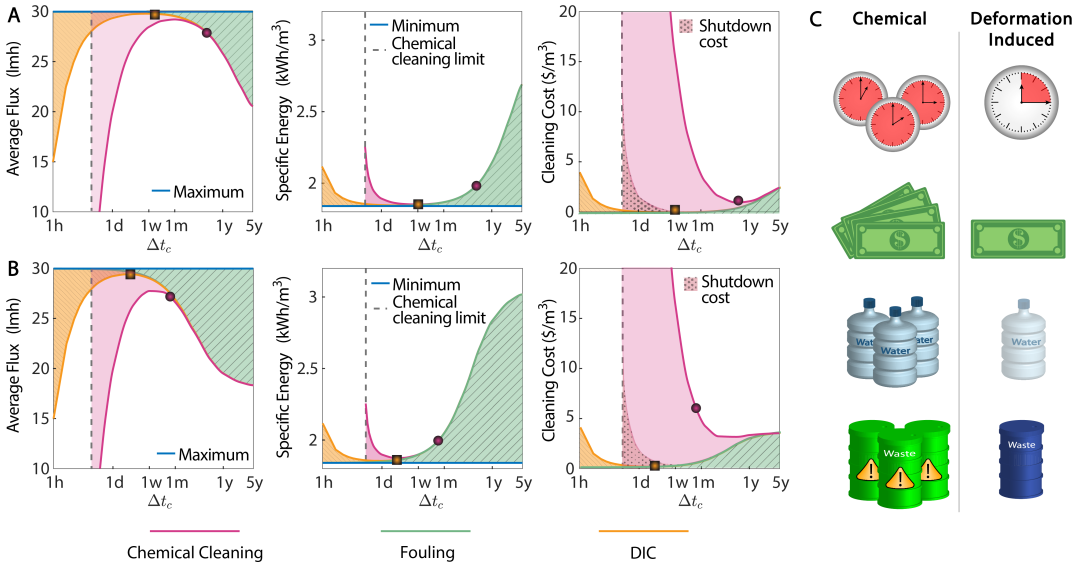

Figure 8. Comparison between chemical and deformation-induced cleaning: A–B) Plots of average flux, specific energy consumption, and cleaning cost as a function of the time between cleanings Δt_c. Typical cleaning operation is represented by a circle, and optimal DIC operation by a square. Shaded regions for chemical cleaning and DIC illustrate the range of losses recoverable by shortening shutdown duration. Shaded regions for fouling, in contrast, illustrate the losses incurred due to flux decline for a given Δt_c. C) A summary of DIC benefits relative to typical cleaning, including shorter shutdowns, less costly operation, in addition to the elimination of both pure water consumption and chemical waste generation.

The results indicate more frequent cleaning is preferable as average fluxes increase and associated specific energies decrease. To that end, one of the main advantages of DIC may lie in its ability to allow operators to reach membrane cleaning frequencies currently prohibitive due to shutdown durations and chemical costs. More importantly, the figures demonstrate that DIC improves plant performance across all metrics considered. Compared to typical chemical cleaning operation, for example, optimal DIC operation can improve the average plant flux by 5–6% while lowering the specific energy consumption by about 10% for both fouling scenarios considered. For the medium-sized plant under consideration, the energy savings could amount to 1.7 GWh/yr, lowering the plant's carbon footprint by 0.12–0.2 kg CO_2/m^3 of pure water depending on the source of fuel utilized [2]. Through the reduction in chemical consumption, likewise, the cleaning cost is significantly lowered relative to typical chemical cleaning operation as illustrated.

To summarize, Figure 8C lists the benefits DIC can provide over chemical methods in tackling membrane cleaning. In addition to lowering shutdown durations and cleaning expenses, DIC eliminates both: permeate water consumption, necessary to prepare the cleaning solution; and chemical waste, generated from the use of cleaning chemicals, that usually requires dilution or treatment and is eventually discharged into the environment [50]. These attributes of DIC have the potential to make desalination more sustainable, environmentally sound, and accessible thus helping to meet the pressing need for fresh water at a time of

rising scarcity worldwide.

We end this section by highlighting important considerations and pathways for future work necessary to achieving widespread DIC implementation in practice. Although this work featured a pneumatic implementation of DIC, still requiring a cleaning shutdown with a precise control of pressure, other implementations of DIC employing different input signals, such as electrical, magnetic, or acoustic, are possible and may even enable continuous RO operation with antifouling capability, ultimately reducing shutdowns even further. Nonetheless, the challenge of developing responsive membranes suitable for such an implementation remains. Another challenge with DIC is scalability as it may prove difficult to control the permeate pressure distribution across SWM modules in trains at industrial scale to deliver effective cleaning without damaging the membranes. To mitigate this challenge, one remedy involves the introduction of multi-staging in DIC in which the cleaning is independently implemented across a number of modules ensuring both appropriate pressure distribution and safe operation. Since this work only experimented on 2.5-inch SWM's, however, future work still needs to investigate applicability to the larger modules deployed industrially.

Furthermore, the effect of spacers on DIC performance requires further exploration. While introducing feed spacers will hinder the progress of fouling due to mixing and the associated increase in shear stresses arising from the flow, our in situ visualizations and experiments coupled with results reported by others [35] indicate that the addition of spacers could act as an impediment to cleaning or foulant removal if those spacers are not optimized for the application. Accordingly, spacer redesign and optimization are expected to play an important role in paving the way for successful DIC implementation.

Research efforts on spacer redesign and optimization should target several criteria to increase the likelihood of optimized DIC performance. First, points of contact between the membrane and spacer provide areas of concentrated stresses that can lead to membrane damage with cyclical deformation. For this reason, spacer redesign efforts should focus on designing spacers featuring smoother edges or softer materials to mitigate the risk of membrane damage upon contact. Research on spacer-free solutions, such as patterned membranes, could also provide an alternative approach to handling this challenge.

Beyond designing spacers that reduce damage or opting for spacer-free solutions, the design of the spacer should also consider the distribution of the interfacial shear stresses that are developed coupled with foulant removal and optimization of the fluid flow around the spacers. Experimental results reported for the SWM indicate long-term buildup of irreversible fouling, a result that may be attributed to foulant aggregates blocking the spacer flow channels. Consequently, investigations into spacer redesign should explore the fluid dynamics of the problem to exploit flow-induced shear stresses in foulant removal, eliminate potential dead zones, and provide a more streamlined path for foulant aggregates to be transported away by the flow. Even though the permeate spacer is not in direct contact with the foulant, its thickness has a potential impact on DIC through constricting the maximum DIC amplitude and should also be considered.

As shown in this work, the effectiveness of DIC diminishes both in regions with minimal deformation and over time due to irreversible fouling. Uneven distribution of fouling due to local variations in flux or the

presence of spacers, for example, may pose additional challenges to cleaning. Since DIC relies on mechanical fatigue to encourage foulant removal, we believe the method would still be effective in the case of uneven foulant distribution provided ample deformation is delivered. While this work has focused on using the method as an alternative to chemical cleaning, DIC may be combined with chemical cleaning in a hybrid harnessing a potential synergy between the two to reach areas potentially less accessible by DIC alone. The result would be an optimized cleaning strategy that simultaneously overcomes these limitations of DIC while reducing chemical consumption and shutdown durations for a plant.

Finally, we mention that unresolved concerns for DIC are that frequent membrane deformation could eventually compromise membrane integrity or may be less effective against other forms of fouling, such as inorganic fouling or biofouling. While our work has demonstrated it is possible to deliver effective mitigation of organic fouling and preserve membrane integrity with proper deformation control, further experimentation under a variety of operating conditions, a larger number of cleaning cycles, and different fouling types remains important before commercial implementation and should be a focus of future investigation.

Future work should also include a study on the effect of shear stresses on the interfacial shear strength between the membrane and other foulant types. For instance, inorganic fouling might respond differently to deformation and the microstructure of the inorganic foulant may also be altered due to the increased surface shear stresses. In the case of a biofilm, the developmental stage and the effect of deformation on quorum sensing are also additional factors worth investigating. More importantly, future work by researchers and membrane fabricators should equally investigate the development of new membrane materials that are more resilient to mechanical stresses. Introducing such materials and new design considerations could eliminate a primary bottleneck to adoption of chemical-free fouling mitigation methods and pave the way for their widespread implementation in practice.

6. Conclusions

Deformation-induced cleaning (DIC) is a novel chemical-free means of removing organic fouling from membranes that may sharply reduce the costs and improve the reliability of water treatment systems. Employing controlled membrane deformation, necessitate the generation of cyclic shear stresses at the membrane-foulant interface, which as a result weakens the adhesion between them, causing cyclic fatigue and eventual removal of the foulant from the membrane layer. This concept is clearly demonstrated with the theoretical analysis of the stresses at the membrane-foulant interface and the experimental results that shows the weakening of the interface after cyclic deformation. In assessing its potential, brackish water desalination experiments were first conducted on a crossflow flat-sheet coupon. Despite the severe fouling, experimental results demonstrate that cleaning can reliably restore flux to greater than 83% of the initial value while preserving membrane integrity. Video footage of DIC, with methylene blue dyed foulants, illustrates the cleaning mechanism in situ. DIC cleaning durations are six-fold lower than traditional chemical-cleaning processes while still delivering comparable cleaning efficiencies. DIC provides a competitive advantage over

chemical methods in addition to being more environmentally sound.

Deformation experiments, run on a no-flow setup, prove the cleaning observed stems from the reduced shear strength, an effect attributed to stress-induced damage to the alginate-membrane interface, with the degradation of the interfacial properties consistent with material fatigue. To further investigate applicability to spiral-wound modules (SWM's), DIC has been applied to commercially-existing modules with feed waters of varying fouling propensities. The cleaning efficiencies achieved demonstrate DIC's applicability to SWM's under a variety of fouling conditions. A case study quantifies the benefits of DIC relative to chemical methods, which stem in part from enabling cleaning frequencies that are cost-prohibitive under current technology. From drastically lowering shutdown durations and cleaning costs to eliminating pure water consumption and chemical waste generation, the benefits of DIC have the potential to move desalination towards greater accessibility and environmental sustainability while meeting the challenge of rising water scarcity globally.

7. Conflicts of interest

There are no conflicts of interest to declare.

8. Acknowledgements

This research is supported by the Abdul Latif Jameel Water and Food Systems Lab (J-WAFS) at the Massachusetts Institute of Technology (MIT) under its seed grant program. Grace Goon acknowledges the postgraduate fellowship from DSO National Laboratories Singapore. Omar Labban acknowledges the financial support received under a J-WAFS Rasikbhai L. Meswani Fellowship for Water Solutions at MIT. Zi Hao Foo is grateful for the financial sponsorship received from the CN Yang Scholars Programme Office, Nanyang Technological University (NTU). The authors also acknowledge Lara Ketonen for contributing to the graphic design of the illustrations presented.

Appendix A. Theoretical background: Deformation mechanics

Appendix A.1. Interfacial shear stresses due to membrane deformation

A few assumptions had to be made to simplify the problem such that an analytical solution for the interfacial stresses can be derived and estimated. Firstly, it was assumed that both the membrane and the alginate film are isotropic, elastic, and homogeneous materials. Next, it was also assumed that the thickness of the membrane-alginate structure is sufficiently small compared to the other dimensions and there was no slip at the surface, such that Kirchoff's plate bending theory still applies. The deformation of the membrane is limited by the clearance between the membrane and the spacer, which is approximately 1 mm. Finally, the boundary condition is assumed to be clamped-clamped and a kinematic assumption satisfying the boundary condition on the deformation, W, of the membrane of length a and width b is applied:

$$W = \frac{W_{max}}{4}\left(\cos\frac{2\pi x}{a} - 1\right)\left(\cos\frac{2\pi y}{b} - 1\right) \tag{A.1}$$

where x and y are the coordinate axes in the width and length directions and the origin is located at the bottom left corner of the membrane, as illustrated in Figure A.1A–B. The mode shpe is depicted in Figure A.1C, with $W_{max} = 0.5$ mm (half of the clearance).

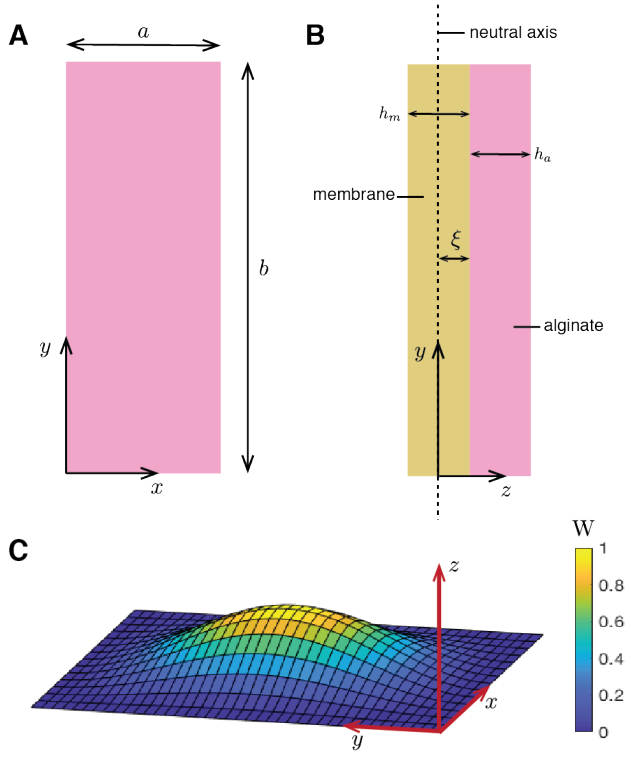

Figure A.1. Setup of the mechanical problem: (A) The in-plane and (B) out-of-plane coordinates and dimensions. (C) The assumed mode shape of the mechanical problem.

Starting with Kirchoff's plate theory, the stress distribution given the deformed shape of the bilayer can be derived. The equations for the in-plane forces are given by:

$$\begin{aligned}\sigma_{xx} &= E\epsilon_{xx} = -\frac{Ez}{1-\nu^2}(\kappa_{xx} + \nu\kappa_{yy}) \\ \sigma_{yy} &= E\epsilon_{yy} = -\frac{Ez}{1-\nu^2}(\kappa_{yy} + \nu\kappa_{xx})\end{aligned} \tag{A.2}$$

Defining $z = 0$ at the neutral axis, the interface is at $z = \xi$, where $\xi = \frac{1}{2}\frac{E_a h_a^2 - E_m h_m^2}{E_a h_a + E_m h_m}$. Tensile stresses on the alginate side can be easily derived by substituting $z = \xi$ and $E = E_a$ into Equation A.2. Substituting Equation A.1 into Equation A.2 yields:

$$\begin{aligned}\sigma_{xx,a} &\approx \frac{E_a z}{1-\nu^2}\frac{W_{max}}{4}\left(\frac{4\pi^2}{a^2}\left(\cos\frac{2\pi y}{b} - 1\right)\cos\frac{2\pi x}{a} + \nu\frac{4\pi^2}{b^2}\left(\cos\frac{2\pi x}{a} - 1\right)\cos\frac{2\pi y}{b}\right) \\ \sigma_{yy,a} &\approx \frac{E_a z}{1-\nu^2}\frac{W_{max}}{4}\left(\frac{4\pi^2}{b^2}\left(\cos\frac{2\pi x}{a} - 1\right)\cos\frac{2\pi y}{b} + \nu\frac{4\pi^2}{a^2}\left(\cos\frac{2\pi y}{b} - 1\right)\cos\frac{2\pi x}{a}\right)\end{aligned} \tag{A.3}$$

Likewise, the stresses on the membrane side can be found by substituting $E = E_m$:

$$\begin{aligned}\sigma_{xx,m} &\approx \frac{E_m z}{1-\nu^2}\frac{W_{max}}{4}\left(\frac{4\pi^2}{a^2}\left(\cos\frac{2\pi y}{b} - 1\right)\cos\frac{2\pi x}{a} + \nu\frac{4\pi^2}{b^2}\left(\cos\frac{2\pi x}{a} - 1\right)\cos\frac{2\pi y}{b}\right) \\ \sigma_{yy,m} &\approx \frac{E_m z}{1-\nu^2}\frac{W_{max}}{4}\left(\frac{4\pi^2}{b^2}\left(\cos\frac{2\pi x}{a} - 1\right)\cos\frac{2\pi y}{b} + \nu\frac{4\pi^2}{a^2}\left(\cos\frac{2\pi y}{b} - 1\right)\cos\frac{2\pi x}{a}\right)\end{aligned} \tag{A.4}$$

For in-plane shear stresses, similarly, beginning from the Kirchhoff's plate equations:

$$\tau_{xy} = \frac{Ez}{1+\nu}\frac{\partial W}{\partial x \partial y} \tag{A.5}$$

Substituting Equation A.1 into Equation A.5:

$$\tau_{xy,a} = \frac{E_a z}{1+\nu} W_{max}\frac{\pi^2}{ab}\sin\frac{2\pi x}{a}\sin\frac{2\pi y}{b} \tag{A.6}$$

$$\tau_{xy,m} = \frac{E_m z}{1+\nu} W_{max}\frac{\pi^2}{ab}\sin\frac{2\pi x}{a}\sin\frac{2\pi y}{b} \tag{A.7}$$

The thin plate assumption implies that the out-of-plane tensile stress is zero everywhere, i.e. $\sigma_{zz} = 0$. However, that does not mean that the out-of-plane shear stresses are zero as well. Instead, the out-of-plane shear stresses can be derived by considering the equilibrium of an infinitesimal element of the plate. The out-of-plane stresses are also continuous across the interface.

$$\begin{aligned}\frac{\partial \sigma_{xx}}{\partial x} + \frac{\partial \tau_{zx}}{\partial z} + \frac{\partial \tau_{xy}}{\partial y} &= 0 \\ \frac{\partial \sigma_{yy}}{\partial y} + \frac{\partial \tau_{zy}}{\partial z} + \frac{\partial \tau_{xy}}{\partial x} &= 0\end{aligned} \tag{A.8}$$

$$\begin{aligned}\frac{\partial \tau_{zx}}{\partial z} &= -\frac{\partial \sigma_{xx}}{\partial x} - \frac{\partial \tau_{xy}}{\partial y} = -\frac{Ez}{1-\nu^2}\left(\frac{\partial^3 W}{\partial x^3} + \nu\frac{\partial W}{\partial x \partial y^2}\right) - \frac{Ez}{1+\nu}\frac{\partial^3 W}{\partial x \partial y^2} = -\frac{Ez}{1-\nu^2}\frac{\partial}{\partial x}\nabla^2 W \\ \frac{\partial \tau_{zy}}{\partial z} &= -\frac{\partial \sigma_{yy}}{\partial y} - \frac{\partial \tau_{xy}}{\partial x} = -\frac{Ez}{1-\nu^2}\left(\frac{\partial^3 W}{\partial y^3} + \nu\frac{\partial W}{\partial y \partial x^2}\right) - \frac{Ez}{1+\nu}\frac{\partial^3 W}{\partial x \partial y^2} = -\frac{Ez}{1-\nu^2}\frac{\partial}{\partial y}\nabla^2 W\end{aligned} \tag{A.9}$$

where,

$$\nabla^2 W = \kappa_{xx} + \kappa_{yy} = \frac{\partial^2 W}{\partial x^2} + \frac{\partial^2 W}{\partial y^2} \tag{A.10}$$

Under a no-flow deformation condition, there are no shear stresses at the surfaces. Integrating directly from the surface to the interface, the shear stresses (i.e. $\tau_{xz}|_{z=-h_m-\xi} = \tau_{xz}|_{z=h_a-\xi} = 0$, $\tau_{yz}|_{z=-h_m-\xi} = \tau_{yz}|_{z=h_a-\xi} = 0$) can be derived. The first two equations below are for the shear stresses in the membrane, and the next two are for the shear stresses in the alginate layer. Like the tensile stresses, the shear stresses at the interface can be derived by substituting $z = \xi$.

$$\begin{aligned}
\tau_{zx,m}(z) &= -\int_{-h_m-\xi}^{z} \frac{E_m}{1-\nu^2}\frac{\partial}{\partial x}\nabla^2 W dz = -\frac{E_m}{1-\nu^2}\frac{\partial}{\partial x}\nabla^2 W \left[\frac{z^2}{2}\right]_{-h_m-\xi}^{z} \\
\tau_{zy,m}(z) &= -\int_{-h_m-\xi}^{z} \frac{E_m}{1-\nu^2}\frac{\partial}{\partial y}\nabla^2 W dz = -\frac{E_m}{1-\nu^2}\frac{\partial}{\partial y}\nabla^2 W \left[\frac{z^2}{2}\right]_{-h_m-\xi}^{z} \\
\tau_{zx,a}(z) &= -\int_{z}^{h_a-\xi} \frac{E_a}{1-\nu^2}\frac{\partial}{\partial x}\nabla^2 W dz = -\frac{E_a}{1-\nu^2}\frac{\partial}{\partial x}\nabla^2 W \left[\frac{z^2}{2}\right]_{z}^{h_a-\xi} \\
\tau_{zy,a}(z) &= -\int_{z}^{h_a-\xi} \frac{E_a}{1-\nu^2}\frac{\partial}{\partial y}\nabla^2 W dz = -\frac{E_a}{1-\nu^2}\frac{\partial}{\partial y}\nabla^2 W \left[\frac{z^2}{2}\right]_{z}^{h_a-\xi}
\end{aligned} \tag{A.11}$$

Thus,

$$\begin{aligned}
\tau_{zx,m}(z) &= -\frac{E_m}{1-\nu^2}\frac{\partial}{\partial x}\nabla^2 W \left[\frac{z^2}{2}\right]_{-h_m-\xi}^{z} \\
&= \frac{E_m}{1-\nu^2} W_{max}\left(\frac{\pi}{a}\right)^3 \left[\sin\frac{2\pi x}{a}\left(\cos\frac{2\pi y}{b} - 1\right) + \frac{a^2}{b^2}\sin\frac{2\pi x}{a}\cos\frac{2\pi y}{b}\right]\left(z^2 - (h_m+\xi)^2\right) \\
\tau_{zy,m}(z) &= -\frac{E_m}{1-\nu^2}\frac{\partial}{\partial y}\nabla^2 W \left[\frac{z^2}{2}\right]_{-h_m-\xi}^{z} \\
&= \frac{E_m}{1-\nu^2} W_{max}\left(\frac{\pi}{b}\right)^3 \left[\sin\frac{2\pi y}{b}\left(\cos\frac{2\pi x}{a} - 1\right) + \frac{b^2}{a^2}\sin\frac{2\pi y}{b}\cos\frac{2\pi x}{a}\right]\left(z^2 - (h_m+\xi)^2\right) \\
\tau_{zx,a}(z) &= -\frac{E_a}{1-\nu^2}\frac{\partial}{\partial x}\nabla^2 W \left[\frac{z^2}{2}\right]_{z}^{h_a-\xi} \\
&= \frac{E_a}{1-\nu^2} W_{max}\left(\frac{\pi}{a}\right)^3 \left[\sin\frac{2\pi x}{a}\left(\cos\frac{2\pi y}{b} - 1\right) + \frac{a^2}{b^2}\sin\frac{2\pi x}{a}\cos\frac{2\pi y}{b}\right]\left((h_a-\xi)^2 - z^2\right) \\
\tau_{zy,a}(z) &= -\frac{E_a}{1-\nu^2}\frac{\partial}{\partial y}\nabla^2 W \left[\frac{z^2}{2}\right]_{z}^{h_a-\xi} \\
&= \frac{E_a}{1-\nu^2} W_{max}\left(\frac{\pi}{b}\right)^3 \left[\sin\frac{2\pi y}{b}\left(\cos\frac{2\pi x}{a} - 1\right) + \frac{b^2}{a^2}\sin\frac{2\pi y}{b}\cos\frac{2\pi x}{a}\right]\left((h_a-\xi)^2 - z^2\right)
\end{aligned} \tag{A.12}$$

Consequently at the interface, $z = \xi$, and as the equations are derived from the equation of equilibrium: $\tau_{int,zx,m} = \tau_{int,zx,a}$ and $\tau_{int,zy,m} = \tau_{int,zy,a}$; the forces across the interface are continuous as mentioned. The shear forces at the interface are therefore imposing the cyclic loading responsible for breaking the adhesive bonds at the interface. It is thus important to estimate the value of shear stresses relative to the shear

strength of the interface.

$$\tau_{int,zx} = \frac{E_a}{1-\nu^2} W_{max} \left(\frac{\pi}{a}\right)^3 \left[\sin\frac{2\pi x}{a}\left(\cos\frac{2\pi y}{b} - 1\right) + \frac{a^2}{b^2}\sin\frac{2\pi x}{a}\cos\frac{2\pi y}{b}\right]\left((h_a-\xi)^2 - \xi^2\right)$$
$$\tau_{int,zy} = \frac{E_a}{1-\nu^2} W_{max} \left(\frac{\pi}{b}\right)^3 \left[\sin\frac{2\pi y}{b}\left(\cos\frac{2\pi x}{a} - 1\right) + \frac{b^2}{a^2}\sin\frac{2\pi y}{b}\cos\frac{2\pi x}{a}\right]\left((h_a-\xi)^2 - \xi^2\right) \quad \text{(A.13)}$$

The parameters in the no-flow experiments are summarized in Table A.1. The Young's moduli are measured using a standard tensile test, while the thicknesses were measured using a vernier caliper. The width and length of the plate are the size of cavity in the module. Given the parameters listed in Table A.1, $\xi \sim 75\,\mu$m, $\tau_{int,zx,max} \sim 5$ Pa and $\tau_{int,zy,max} \sim 1$ Pa. As the pressure is applied cyclically, the deformation, and hence, interfacial shear stress are cyclical, with a load of $\Delta\tau_{int,zx} = 2\tau_{int,zx,max} \sim 10$ Pa.

The interfacial shear strength was measured to be about $40 - 100$ Pa, which means that this cyclic load was only $10 - 20$ % of the strength value. Based on the reduction in shear strength observed in the main manuscript, the cyclic shear levels were above the threshold stress at which fatigue occurs, and therefore, cyclic fatigue of the interface occured.

Table A.1. Material parameters

Parameter	Value
E_a	30 ± 2 kPa
E_m	220 ± 10 MPa
h_a	410 ± 10 μm
h_m	150 ± 10 μm
a	0.030 ± 0.001 m
b	0.080 ± 0.001 m
W_{max}	0.5 mm
ν	0.3

Appendix A.2. Failure criterion derivation

Appendix A.2.1. Based on the equilibrium assumption

The force, F_s, required to shear off a layer of alginate (of attached section of width a and length b, and height h_a) from the membrane is simply given by the product of the yield shear strength, τ_y, and the area of the alginate in contact with the membrane:

$$F_s = \tau_y ab \quad \text{(A.14)}$$

For progressive delamination of the alginate layer, the per unit strain energy release rate must equate the adhesion energy, Γ. The expression used in Golovin et al. [46] assumes tensile force in the foulant layer:

$$\Gamma = \frac{1}{2}\frac{{\sigma_t}^2 h_a}{E_a} \tag{A.15}$$

where σ_t is the tensile stress in the alginate, E_a is the elastic modulus of the alginate, and h_a is the thickness of the alginate layer. The tensile stress is given by the applied force, F_t, divided by the cross section of the alginate layer:

$$\sigma_t = \frac{F_t}{a h_a} \tag{A.16}$$

Substituting into Equation A.15,

$$F_t = \sqrt{2\Gamma E_a h_a a^2} \tag{A.17}$$

Equating F_s and F_t, the critical length, $b = L_c$, at which the transition between failure due to shear strength and failure due to crack propagation occurs is given by:

$$\begin{aligned} \tau_y L_c a &= \sqrt{2\Gamma E_a h_a a^2} \\ L_c &= \sqrt{\frac{2\Gamma E_a h_a}{{\tau_y}^2}} \end{aligned} \tag{A.18}$$

In this case, when $b < L_c$, the delamination of the alginate layer is driven by the shear strength criterion. When $b > L_c$, the delamination is driven by adhesion energy.

Appendix A.2.2. Based on the kinematic assumption

The failure criterion derivation in the Section Appendix A.2.1 is accurate for a structure with an equilibrium assumption, i.e. force controlled deformation. For a structure that is deformed with a displacement limitation, the above derivation of the criteria has to be reevaluated with new expressions of shear stresses and strain energy release rate.

As the in-plane tensile stresses are at least an order of magnitude bigger than the other stresses, the contribution of the other stress components may be neglected. The in-plane tensile stresses are provided here for convenience:

$$\begin{aligned} \sigma_{xx,a} &\approx \frac{E_a z}{1-\nu^2}\frac{W_{max}}{4}\left(\frac{4\pi^2}{a^2}\left(\cos\frac{2\pi y}{b}-1\right)\cos\frac{2\pi x}{a} + \nu\frac{4\pi^2}{b^2}\left(\cos\frac{2\pi x}{a}-1\right)\cos\frac{2\pi y}{b}\right) \\ \sigma_{yy,a} &\approx \frac{E_a z}{1-\nu^2}\frac{W_{max}}{4}\left(\frac{4\pi^2}{b^2}\left(\cos\frac{2\pi x}{a}-1\right)\cos\frac{2\pi y}{b} + \nu\frac{4\pi^2}{a^2}\left(\cos\frac{2\pi y}{b}-1\right)\cos\frac{2\pi x}{a}\right) \end{aligned} \tag{A.19}$$

Likewise, the shear stresses generated at the interface are provided:

$$\begin{aligned} \tau_{int,zx} &= \frac{E_a}{1-\nu^2}W_{max}\left(\frac{\pi}{a}\right)^3\left[\sin\frac{2\pi x}{a}\left(\cos\frac{2\pi y}{b}-1\right) + \frac{a^2}{b^2}\sin\frac{2\pi x}{a}\cos\frac{2\pi y}{b}\right]\left((h_a-\xi)^2-\xi^2\right) \\ \tau_{int,zy} &= \frac{E_a}{1-\nu^2}W_{max}\left(\frac{\pi}{b}\right)^3\left[\sin\frac{2\pi y}{b}\left(\cos\frac{2\pi x}{a}-1\right) + \frac{b^2}{a^2}\sin\frac{2\pi y}{b}\cos\frac{2\pi x}{a}\right]\left((h_a-\xi)^2-\xi^2\right) \end{aligned} \tag{A.20}$$

For simplification of the derivation, assume $a \sim b = L$:

$$\sigma_{xx,a} \sim \sigma_{yy,a} \sim \frac{E_a z}{1-\nu^2}\frac{W_{max}}{4}\left(\frac{4\pi^2}{L^2}\left(\cos\frac{2\pi y}{L}-1\right)\cos\frac{2\pi x}{L}+\nu\frac{4\pi^2}{L^2}\left(\cos\frac{2\pi x}{L}-1\right)\cos\frac{2\pi y}{L}\right) \tag{A.21}$$

$$\tau_{int,zx} \sim \tau_{int,zy} \sim \frac{E_a}{1-\nu^2}W_{max}\left(\frac{\pi}{L}\right)^3\left[\sin\frac{2\pi x}{L}\left(\cos\frac{2\pi y}{L}-1\right)+\sin\frac{2\pi x}{L}\cos\frac{2\pi y}{L}\right]\left((h_a-\xi)^2-\xi^2\right) \tag{A.22}$$

The order of magnitude of the strain energy release rate due to the in-plane tensile stresses is given by:

$$\Gamma = \frac{1}{2}\int_{\xi}^{h_a+\xi}\boldsymbol{\sigma}:\boldsymbol{\epsilon}\,dz = \frac{1}{2E_a}\int_{\xi}^{h_a+\xi}\sigma_{ij}\sigma_{ij}dz \tag{A.23}$$

$$\sim \frac{1}{2E_a}\int_{\xi}^{h_a+\xi}\sigma_{xx,a}^2+\sigma_{yy,a}^2 dz \approx \frac{1}{E_a}\int_{\xi}^{h_a+\xi}\sigma_{xx,a}^2 dz \tag{A.24}$$

Considering only the maximum strain energy release rate and shear strength, by setting $\cos\frac{2\pi y}{L}=-1$ and $\cos\frac{2\pi x}{L}=-1$

$$\Gamma_{max} \sim \frac{1}{E_a}\left(\frac{E_a z}{1-\nu^2}\frac{W_{max,\Gamma}}{4}\left(\frac{8\pi^2}{L^2}+\nu\frac{8\pi^2}{L^2}\right)\right)^2\int_{\xi}^{h_a+\xi}z^2dz \tag{A.25}$$

$$= \frac{E_a}{(1-\nu^2)^2}W_{max,\Gamma}^2\frac{4\pi^4}{L^4}(1+\nu)^2\int_{\xi}^{h_a+\xi}z^2dz \tag{A.26}$$

$$= \frac{E_a}{(1-\nu^2)^2}W_{max,\Gamma}^2\frac{4\pi^4}{L^4}(1+\nu)^2\frac{1}{3}\left[(h_a+\xi)^3-\xi^3\right] \tag{A.27}$$

$$= \frac{E_a}{(1-\nu^2)^2}W_{max,\Gamma}^2\frac{4\pi^4}{L^4}(1+\nu)^2 C_G \tag{A.28}$$

where $C_G = \frac{1}{3}\left[(h_a+\xi)^3-\xi^3\right]$,

$$\begin{aligned}\tau_{int,zx,max} &\sim \frac{E_a}{1-\nu^2}W_{max,\tau}\left(\frac{\pi}{L}\right)^3 3h_a(h_a-2\xi)\\ &= \frac{E_a}{1-\nu^2}W_{max,\tau}\left(\frac{\pi}{L}\right)^3 C_\tau\end{aligned} \tag{A.29}$$

where $C_\tau = 3h_a(h_a-2\xi)$.

To find the deformation required to initiate failure at the interface because the shear stresses exceed the shear strength, equate $\tau_{int,zx,max} = \tau_y$:

$$\begin{aligned}W_{max,\tau} &\sim \tau_y\frac{1-\nu^2}{E_a C_\tau}\left(\frac{L}{\pi}\right)^3\\ W_{max,\tau}^2 &\sim \left(\tau_y\frac{1-\nu^2}{E_a C_\tau}\left(\frac{L}{\pi}\right)^3\right)^2\end{aligned} \tag{A.30}$$

Similarly, to find the maximum deformation required to initiate failure at the interface because there is sufficient strain energy stored in the film to overcome the adhesion energy, equate $\Gamma_{max} = \Gamma$:

$$W_{max,\Gamma}^2 \sim \Gamma \frac{(1-\nu^2)^2}{E_a C_G (1+\nu)^2} \frac{L^4}{4\pi^4} \tag{A.31}$$

At the critical characteristic length of the bonded segment, $L = L_c$, the mechanism switches from failure by exceeding the interfacial shear strength to the release of strain energy in the film, $W_{max,\tau}^2 = W_{max,\Gamma}^2$.

$$\begin{aligned}
\Gamma \frac{(1-\nu^2)^2}{E_a C_G (1+\nu)^2} \frac{L_c^4}{4\pi^4} &\sim \tau_y^2 \frac{(1-\nu^2)^2}{E_a^2 C_\tau^2} \left(\frac{L_c}{\pi}\right)^6 \\
\Gamma \frac{1}{C_G (1+\nu)^2} \frac{1}{4} &\sim \tau_y^2 \frac{1}{E_a C_\tau^2} \left(\frac{L_c}{\pi}\right)^2 \\
\left(\frac{L_c}{\pi}\right)^2 &\sim \frac{E_a \Gamma C_\tau^2}{4 C_G (1+\nu)^2} \frac{1}{\tau_y^2} \\
L_c^2 &\sim \frac{\pi^2 C_\tau^2}{4 C_G (1+\nu)^2} \frac{E_a \Gamma}{\tau_y^2} \\
L_c &\sim \sqrt{\frac{\pi^2 C_\tau^2}{8 C_G (1+\nu)^2} \frac{2 E_a \Gamma}{\tau_y^2}} = \frac{k}{2(1+\nu)} \sqrt{\frac{2 E_a \Gamma h_a}{\tau_y^2}}
\end{aligned} \tag{A.32}$$

which is a similar form to Equation A.18, with a prefactor, $\frac{k}{2(1+\nu)}$, where $k = \sqrt{\frac{\pi^2 C_\tau^2}{2 h_a C_G}}$, where C_τ and C_G are determined by the cross sectional material properties and dimensions of the bilayer.

The value of the shear strength varies widely between $40 - 100$ Pa, and an average value of the measured shear strength is used as a representative value. Substituting the values in Table A.1, the interfacial adhesion energy, $\Gamma = 0.52 \pm 0.02$ J/m^2, and interfacial shear strength, $\tau_y = 70 \pm 30$ Pa, into Equation A.32, the critical length is found to vary between $0.09 - 0.19$ m. In the experiment, the feed spacer cuts the foulant layer into smaller pieces and the length scale in question is the size of the spacer grid, which is 2.00 $\pm$ 0.05 mm. Therefore, we have L$< L_c$, meaning that the alginate detached from the membrane due to the shear strength criterion.

However, it should also be noted that when the foulant is cut into smaller pieces, each individual piece has to over come the shear strength or each alginate pieces has to store sufficient strain energy to overcome the adhesion energy. The critical length scale would be extremely difficult to express, but the maximum displacement required for the interfacial shear stress at a particular location to exceed the shear strength or for the strain energy stored in the film to exceed the adhesion energy can be easily computed, as presented in Figure A.2a and b. The mode of failure that requires the lower deformation will be the local failure mode, presented in Figure A.2c. The red section indicates shear failure while the blue section indicates strain energy release rate failure. Visually, it can be inferred that most of the foulant-membrane interface fails by shear, with the exception of a few spots where the shear stresses are low. Thus the critical bonded length presented above is a sufficient estimate as most of the foulant pieces would fail by shear.

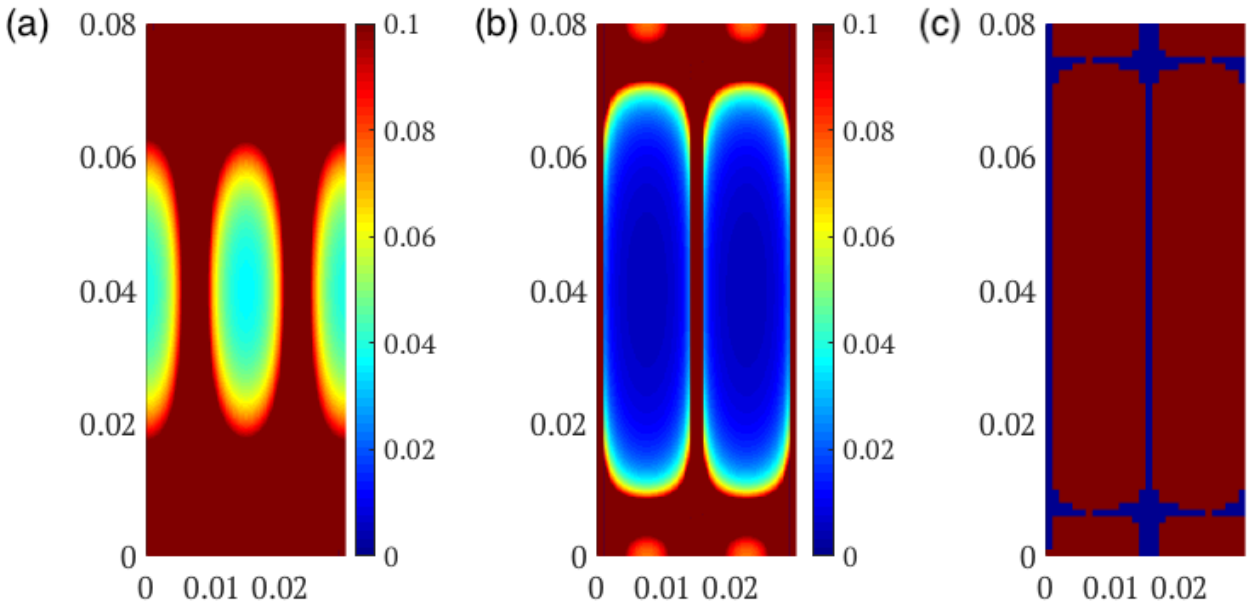

Figure A.2. The required maximum deformation for local failure (a) by strain energy release rate (b) by shear failure. (c) red indicates shear failure while blue indicates strain energy release failure

In the case when the spacer is not present, the width of the attached area is 0.03 m, while the length is 0.08 m. Hence, the dominant failure criterion in the width direction is the shear strength criterion, and it could be either criterion in the length direction depending on the membrane properties. However, it should also be noted that during deformation, stresses in the x direction are higher than those in the y direction, and thus, it would be likely to fail by the shear strength criterion. The case where the spacer is not present is unlikely to present itself in a spiral-wound, where a feed spacer is designed to create the feed channel.

Appendix A.2.3. Lap-shear tests

The criterion stated in Equation A.18 can be used when the system is subjected to stresses induced by deformation as it is during the deformation stage in the cross-flow experiments, no-flow experiments, or when a tensile force is directly applied to the alginate layer. In the case of the lap shear experiment, the strain energy release rate is expressed as:

$$\Gamma_s = \frac{1}{2}\frac{{\sigma_s}^2 h}{E} \tag{A.33}$$

Equating $\sigma_t = \sigma_y$ and $\Gamma_s = \Gamma$, we have the following thickness criterion:

$$h_c = \frac{2\Gamma E}{{\sigma_y}^2}, \tag{A.34}$$

above which ($h > h_c$) the interface fails via the strain energy criterion, and below which ($h < h_c$) the interface fails via the shear strength criterion. Substituting the values stated in Table A.1, the critical thickness is

found to vary between $2.8 - 21.6$ m, which is significantly larger than the thickness of the alginate layer. Consequently, it can be assumed to fail by shear strength. The shear strength could then be easily derived from the force measured during the lap shear test.

Appendix B. Case study: Model derivations and assumptions

In the case study presented, a brackish water (15,168 mg/kg) desalination plant with a 24,000 m^3/day capacity was adopted for analysis. Plant design specifications and projected lifetime were matched to those reported by Atab et al. [47]. For consistency, membrane and spacer properties were matched to the FILMTEC TW30-2514 membrane [48] adopted herein, and an 8-inch module geometry was assumed in-line with industry standards. The plant specifications are summarized in Table B.2 for reference.

Modeling assumptions for RO were generally in tandem with those presented by Wei et al. [51]. Specifically, the feed water was chosen to be NaCl and water, perfect salt rejection by the membranes was assumed, and 8 membrane elements or modules were allocated to every pressure vessel. For simplicity, concentration polarization was neglected together with the energy consumed by the circulation pump during production. Furthermore, simulations executed did not account for capital expenses or costs associated with waste treatment or disposal. These simulations were run for the entire duration of the membranes' projected lifetime.

Table B.2. Nominal specifications of modeled desalination plant. [47, 48, 6, 49]

Specification	Nominal Value
Capacity	24,000 m^3/day
Feed salinity	15,168 mg/kg
Recovery ratio	45%
Target average system flux	30 LMH
Feed pressure	25 bars
Cleaning pressure drop	4.5 bars
Membrane pure water permeability	3.25 LMH/bar
Feed spacer thickness	28 mils
Module size (active area)	8-inch (33.9 m^2)
Module feed channel effective volume	12 L
Number of modules	984
Membrane lifetime	5 years

As shown in Table B.2, the recovery ratio for the desalination plant was selected to be 45% following Atab et al. [47], and the target average system flux was specified to be 30 LMH, a value common in brackish water RO. The required membrane area and corresponding number of modules were related to the plant capacity, average system flux, and module active area (specified by the manufacturer) according to:

$$N_m = \frac{\dot{Q}_p}{A_m \bar{J}_{sys}} \tag{B.1}$$

Moreover, the inlet feed flow rate per pressure vessel was then determined from the plant production capacity, recovery ratio, and number of pressure vessels.

The inlet feed pressure necessary to match the design was estimated following the iterative procedure outlined by Wei et al. [51]. Specifically, every element was modeled independently through the application of conservation laws. The flux across an element was calculated according to:

$$J_i = A_m(\Delta P - \Delta\Pi_i) \tag{B.2}$$

where J is the flux, the index i denotes the element number, ΔP is the applied pressure difference, and the osmotic pressure difference $\Delta\Pi_i$ was calculated via Pitzer's model [52]. Based on the assumption of perfect salt rejection, the salinity at the outlet of every element was calculated to be:

$$s_{b,i} = \frac{s_{f,i}}{1 - RR_i} \tag{B.3}$$

In this equation, $s_{f,i}$, $s_{b,i}$, and RR_i denote the respective feed salinity, brine salinity, and recovery ratio for the i^{th} element in the vessel under consideration. Following the iterative scheme, the inlet feed pressure necessary was calculated to be 25 bars (Table B.2).

To capture the economics of plant operation, a model describing the fouling and cleaning processes becomes necessary. Given the scope of the study, a simplified model, representing fouling and flux decline by an exponentially decaying function, has been adopted:

$$\bar{J}^*(t) = D\big(\bar{J}^*_{min} + (1 - \bar{J}^*_{min})e^{-t/\tau_c}\big) \tag{B.4}$$

The model has been adopted elsewhere to describe organic fouling in reverse osmosis [53] and is derived based on the deposition-minus-removal model presented in the heat exchanger literature. In Eq. B.4, $\bar{J}^* = \frac{\bar{J}}{J_{max}}$, where $\bar{J}$ is the average system flux in LMH and $J_{max} = \bar{J}_{sys} = 30$ LMH, refers to the normalized average system flux as a function of elapsed time, t, at the beginning of each production cycle. $\bar{J}^*_{min}$ is the minimum normalized average system flux taken to be 0.6 [53], τ_c is a positive time constant capturing the fouling rate, and D is the membrane degradation rate set herein to unity for simplicity.

Furthermore, the total permeate produced by the plant is calculated according to:

$$Q_{tot} = \sum_{j=1}^{N}\left(A\ J_{max}\int_0^{\Delta t_j}\bar{J}^*(t)dt\right) \tag{B.5}$$

where A is the total membrane active area, N is the number of production cycles, and Δt_j represents the corresponding cycle duration. The specific energy consumption was estimated as the ratio of the total energy consumption to the total permeate produced:

$$e = \frac{\dot{W}\,t_{op}}{Q_{tot}} = \frac{\dot{Q}\Delta P}{Q_{tot}}\left(\sum_{j=1}^{N}\Delta t_j\right) \tag{B.6}$$

where $\dot{W}$ is the power delivered by the high-pressure pump, t_{op} is the total operation time, $\dot{Q}$ is the intake feed flow rate, and ΔP is the pressure difference across the high-pressure pump.

In addition to modeling plant operation during production, a complete assessment should not ignore the costs associated with the cleaning procedure. First, the average permeate loss incurred with the production halt may be estimated as:

$$Q_{sh} = -Q_{tot}\Big(t_{sh}/t_{op}\Big) \tag{B.7}$$

where t_{sh} is the total shutdown time taken to be 30 mins/cycle for DIC and 8 hours/cycle for chemical cleaning.

To prepare the chemical cleaning solution, permeate water is typically used, contributing further to the permeate loss incurred in chemical cleaning. In this model, the permeate consumption associated with chemical cleaning was calculated according to Eq. B.8:

$$Q_{cc} = 2V_m N_m \tag{B.8}$$

where V_m is the effective volume of the feed channel per element or module, and N_m is the total number of modules in operation. Following the chemical cleaning protocol recommended in practice [39], this assumption allocates one volume to displacing the residual feed and another to cleaning the module. The volume V_m was calculated taking into consideration the membrane active area and the feed spacer thickness (refer to Table B.2 for details):

$$V_m = \frac{1}{2} A_m t_s \tag{B.9}$$

Here, t_s refers to the spacer thickness and a factor of one-half is introduced to account for the SWM membrane placement in which membranes are arranged in bilayers sharing the same spacer.

To allow for a meaningful comparison between DIC and chemical cleaning, the different costs associated with cleaning may be combined into a single metric, the cost of cleaning, C. The cost of cleaning was taken as the sum of the costs associated with any chemicals/water consumption, energy consumption by the circulation pump, and the lost productivity attributed to shutdown as calculated in Eq. B.7:

$$C = \frac{Q_{cc}(\pi_{cc} + \pi_w) + Q_{sh}\pi_w + t_c(\dot{Q}_c \Delta P_L)\pi_e}{Q_{tot}} \tag{B.10}$$

where π_{cc}, π_w, and π_e denote the costs associated with cleaning chemicals, pure water, and energy consumption. Moreover, $\dot{Q}_c$ is the flow rate and ΔP_L is the pressure drop incurred during cleaning, while t_c refers to the time during which circulation was maintained for cleaning ($t_c = t_{sh}$ for DIC and $t_c = 3N$ hr for chemical cleaning, where N is the total number of production cycles over the membranes' projected lifetime). Given the higher velocities involved during cleaning, furthermore, the pressure drop incurred across a vessel by the circulation pump was taken to be 4.5 bars [6]. Based on the recommendation of the manufacturer, the flow rate during cleaning was taken to be $\dot{Q}_c = 3\dot{Q}$.

For chemical cleaning, the cost of chemicals reported by Fritzmann et al. [7] ($\pi_{cc} = \$0.041/\mathrm{m}^3$ permeate) was initially adopted for standard operation, and then normalized per unit volume of chemicals consumed for later comparisons when more frequent cleaning cycles were executed. The cost of purified water adopted ($\pi_w = \$0.41/\mathrm{m}^3$) accounts for the total variable costs associated with water production (energy, labor, and

overhead costs), while the cost of energy consumed by the circulation pump was taken to be $\pi_e = \$0.08/\text{kWh}$ [54].

To quantify the benefits of DIC over chemical cleaning, a standard chemical cleaning protocol, executed twice annually, was initially established as the benchmark [6] and relative savings were calculated. The cleaning frequency was later varied to investigate its effect on overall plant productivity. Additionally, feeds with varying fouling propensities were considered by varying the time constant τ_c to assess the potential of DIC under different operation conditions. $\bar{J}^*_{min}$ was assumed constant to simplify the analysis.

Nomenclature

Roman Symbols

a	Width of the membrane active area (Constant), m
A	Total membrane active area, m^2
A_m	Membrane active area per module, m^2
b	Length of the membrane active area (Constant), m
C	Cost of cleaning, \$/m^3
e	Specific energy consumption, kWh/m^3
F	Force, N
$\bar{J}$	Average system flux, LMH
$\bar{J}^*$	Normalized average system flux
$\bar{J}_{sys}$	Target average system flux, 30 LMH
D	Membrane degradation rate
E	Young's Modulus, Pa
h	Thickness, m
L	length of the membrane-alginate interface in critical length criterion calculation, m
N	Number of production cycles over the membranes' projected lifetime
N_m	Number of modules
$\dot{Q}$	Feed flow rate, m^3/hr
$\dot{Q}_p$	Permeate flow rate, m^3/hr
Q_{tot}	Total permeate produced, m^3
Q_{sh}	Permeate lost during shutdown, m^3
RR	Recovery ratio
s	Salinity, mg/kg
t	Time, hr
t_c	Cleaning time with pump circulation, hr
t_s	Spacer thickness, m
V_m	Feed channel effective volume (per module), m^3
w	Width of the membrane in critical length criterion calculation, m
$\dot{W}$	Pumping power, kW
W	Assumed deformation shape of membrane, m
W_{max}	Maximum deformation of membrane, m
x	In-plane horizontal coordinate, m
y	In-plane vertical coordinate, m
z	Out-of-plane coordinate, m

Greek Symbols

ΔP	Applied pressure difference, Pa
$\Delta\Pi$	Osmotic pressure difference, Pa
Γ	Adhesion energy, Jm^{-2}
κ	Curvature, m^{-1}
π	Cost factor, \$/unit
ν	Poisson ratio
σ	Tensile stress, Pa
τ	Shear stress, Pa
τ_c	Fouling time constant, hr
ξ	Distance of interface from neutral axis, m

Subscripts

a	alginate
b	brine
c	critical value
cc	chemical cleaning
e	energy
f	feed
i	element number in a pressure vessel
ij	where $i, j = x, y$ or z indicates the components of curvatures or stresses. For stresses: i indicates the direction and j indicates the face the stresses act on.
L	pressure loss
m	membrane
min	minimum
op	total operating time
s	shear criterion
sh	total shutdown time
s	tensile criterion
w	pure water
y	yield condition

References

[1] M. M. Mekonnen, A. Y. Hoekstra, Four billion people facing severe water scarcity, Science Advances 2 (2). doi:10.1126/sciadv.1500323.

[2] J. H. Lienhard, G. P. Thiel, D. M. Warsinger, L. D. Banchik, Low carbon desalination: Status and research, development, and demonstration needs, Report of a workshop conducted at the Massachusetts Institute of Technology in association with the Global Clean Water Desalination Alliance, MIT Abdul Latif Jameel World Water and Food Security Lab, Cambridge, Massachusetts, 2016.
URL http://hdl.handle.net/1721.1/105755

[3] A. Bajpayee, T. Luo, A. Muto, G. Chen, Very low temperature membrane-free desalination by directional solvent extraction, Energy & Environmental Science 4 (2011) 1672–1675. doi:10.1039/C1EE01027A.

[4] D. Cohen-Tanugi, R. K. McGovern, S. H. Dave, J. H. Lienhard, J. C. Grossman, Quantifying the potential of ultra-permeable membranes for water desalination, Energy & Environmental Science 7 (2014) 1134–1141. doi:10.1039/C3EE43221A.

[5] X. Zhou, F. Zhao, Y. Guo, Y. Zhang, G. Yu, A hydrogel-based antifouling solar evaporator for highly efficient water desalination, Energy & Environmental Science 11 (2018) 1985–1992. doi:10.1039/C8EE00567B.

[6] N. Voutchkov, Desalination engineering: Planning and design, McGraw Hill, 2013.

[7] C. Fritzmann, J. Löwenberg, T. Wintgens, T. Melin, State-of-the-art of reverse osmosis desalination, Desalination 216 (1) (2007) 1 – 76. doi:10.1016/j.desal.2006.12.009.

[8] A. Antony, G. Leslie, Degradation of polymeric membranes in water and wastewater treatment, in: Advanced Membrane Science and Technology for Sustainable Energy and Environmental Applications, Woodhead Publishing Series in Energy, Woodhead Publishing, 2011, pp. 718 – 745. doi:10.1533/9780857093790.5.718.

[9] N. Avraham, C. Dosoretz, R. Semiat, Osmotic backwash process in RO membranes, Desalination 199 (1) (2006) 387 – 389, Euromembrane 2006. doi:10.1016/j.desal.2006.03.088.

[10] MICRODYN-NADIR, MICRODYN SpiraSep 960 Ultrafiltration Modules Product Manual, 2019.

[11] O. Labban, G. Goon, Z. H. Foo, X. Zhao, J. H. Lienhard, Osmotically-induced cleaning of fouled reverse osmosis membranes in desalination, IDA World Congress on Desalination and Water Reuse, Dubai, UAE, 20-24 Oct. 2019.
URL https://hdl.handle.net/1721.1/123205

[12] B. Liberman, I. Liberman, Replacing membrane CIP by Direct Osmosis cleaning, International Desalination and Water Reuse Quarterly 15 (2) (2005) 28.

[13] B. Liberman, Direct osmosis cleaning, US Patent 7,563,375 (Jul. 21 2009).

[14] J.-J. Qin, M. H. Oo, K. A. Kekre, B. Liberman, Development of novel backwash cleaning technique for reverse osmosis in reclamation of secondary effluent, Journal of Membrane Science 346 (1) (2010) 8 – 14. doi:10.1016/j.memsci.2009.08.011.

[15] S. Lee, M. Elimelech, Salt cleaning of organic-fouled reverse osmosis membranes, Water Research 41 (5) (2007) 1134 – 1142. doi:10.1016/j.watres.2006.11.043.

[16] A. Sagiv, R. Semiat, Backwash of RO spiral wound membranes, Desalination 179 (1) (2005) 1 – 9, Membranes in Drinking and Industrial Water Production. doi:10.1016/j.desal.2004.11.050.

[17] A. M. Farooque, S. Al-Jeshi, M. O. Saeed, A. Alreweli, Inefficacy of osmotic backwash induced by sodium chloride salt solution in controlling SWRO membrane fouling, Applied Water Science 4 (4) (2014) 407–424. doi:10.1007/s13201-014-0158-x.

[18] F. Zamani, J. W. Chew, E. Akhondi, W. B. Krantz, A. G. Fane, Unsteady-state shear strategies to enhance mass-transfer for the implementation of ultrapermeable membranes in reverse osmosis: A review, Desalination 356 (2015) 328–348. doi:10.1016/j.desal.2014.10.021.

[19] A. Subramani, J. DeCarolis, W. Pearce, J. G. Jacangelo, Vibratory shear enhanced process (VSEP) for treating brackish water reverse osmosis concentrate with high silica content, Desalination 291 (2012) 15–22. doi:10.1016/j.desal.2012.01.020.

[20] M. Y. Jaffrin, Dynamic filtration with rotating disks, and rotating and vibrating membranes: an update, Current Opinion in Chemical Engineering 1 (2) (2012) 171–177. doi:10.1016/j.coche.2012.01.002.

[21] W. Shi, M. M. Benjamin, Membrane interactions with NOM and an adsorbent in a vibratory shear enhanced filtration process (VSEP) system, Journal of Membrane Science 312 (1-2) (2008) 23–33. doi:10.1016/j.memsci.2007.12.031.

[22] G. Genkin, T. Waite, A. Fane, S. Chang, The effect of vibration and coagulant addition on the filtration performance of submerged hollow fibre membranes, Journal of Membrane Science 281 (1-2) (2006) 726–734. doi:10.1016/j.memsci.2006.04.048.

[23] A. Kola, Y. Ye, A. Ho, P. Le-Clech, V. Chen, Application of low frequency transverse vibration on fouling limitation in submerged hollow fibre membranes, Journal of Membrane Science 409 (2012) 54–65. doi:10.1016/j.memsci.2012.03.017.

[24] S. Low, H. H. Juan, L. K. Siong, A combined VSEP and membrane bioreactor system, Desalination 183 (1-3) (2005) 353–362. doi:10.1016/j.desal.2005.04.028.

[25] A. Kola, Y. Ye, P. Le-Clech, V. Chen, Transverse vibration as novel membrane fouling mitigation strategy in anaerobic membrane bioreactor applications, Journal of Membrane Science 455 (2014) 320–329. doi:10.1016/j.memsci.2013.12.078.

[26] F. Zamani, A. W. Law, A. Fane, Hydrodynamic analysis of vibrating hollow fibre membranes, Journal of Membrane Science 429 (2013) 304–312. doi:10.1016/j.memsci.2012.11.024.

[27] T. Li, A. W.-K. Law, A. G. Fane, Submerged hollow fibre membrane filtration with transverse and longitudinal vibrations, Journal of Membrane Science 455 (2014) 83–91. doi:10.1016/j.memsci.2013.12.042.

[28] J. Bae, I. Baek, H. Choi, Efficacy of piezoelectric electrospun nanofiber membrane for water treatment, Chemical Engineering Journal 307 (2017) 670–678. doi:10.1016/j.cej.2016.08.125.

[29] D. Chen, C. Pomalaza-Ráez, A self-cleaning piezoelectric PVDF membrane system for filtration of kaolin suspension, Separation and Purification Technology 215 (2019) 612–618. doi:10.1016/j.seppur.2018.12.082.

[30] M. Mertens, M. Quintelier, I. F. Vankelecom, Magnetically induced membrane vibration (MMV) system for wastewater treatment, Separation and Purification Technology 211 (2019) 909–916. doi:10.1016/j.seppur.2018.08.060.

[31] B. Wu, Y. Zhang, Z. Mao, W. S. Tan, Y. Z. Tan, J. W. Chew, T. H. Chong, A. G. Fane, Spacer vibration for fouling control of submerged flat sheet membranes, Separation and Purification Technology 210 (2019) 719–728. doi:10.1016/j.seppur.2018.08.062.

[32] Y. Z. Tan, Z. Mao, Y. Zhang, W. S. Tan, T. H. Chong, B. Wu, J. W. Chew, Enhancing fouling mitigation of submerged flat-sheet membranes by vibrating 3D-spacers, Separation and Purification Technology 215 (2019) 70–80. doi:10.1016/j.seppur.2018.12.085.

[33] W. Li, X. Su, A. Palazzolo, S. Ahmed, E. Thomas, Reverse osmosis membrane, seawater desalination with vibration assisted reduced inorganic fouling, Desalination 417 (2017) 102–114. doi:10.1016/j.desal.2017.05.016.

[34] H. Gomaa, S. Rao, Analysis of flux enhancement at oscillating flat surface membranes, Journal of Membrane Science 374 (1-2) (2011) 59–66. doi:10.1016/j.memsci.2011.03.011.

[35] E. W. Tow, M. M. Rencken, J. H. Lienhard, In situ visualization of organic fouling and cleaning mechanisms in reverse osmosis and forward osmosis, Desalination 399 (2016) 138 – 147. doi:10.1016/j.desal.2016.08.024.

[36] O. Orgad, Y. Oren, S. L. Walker, M. Herzberg, The role of alginate in pseudomonas aeruginosa EPS adherence, viscoelastic properties and cell attachment, Biofouling 27 (7) (2011) 787–798. doi:10.1080/08927014.2011.603145.

[37] A. W. Decho, T. Gutierrez, Microbial extracellular polymeric substances (EPSs) in ocean systems, Frontiers in Microbiology 8 (2017) 922. doi:10.3389/fmicb.2017.00922.

[38] C. Xu, W.-C. Chin, P. Lin, H. Chen, M.-H. Chiu, D. C. Waggoner, W. Xing, L. Sun, K. A. Schwehr, P. G. Hatcher, et al., Comparison of microgels, extracellular polymeric substances (EPS) and transparent exopolymeric particles (TEP) determined in seawater with and without oil, Marine Chemistry (2019) 103667doi:10.1016/j.marchem.2019.103667.

[39] DOW FILMTEC Membranes: Cleaning Procedures for DOW FILMTEC FT30 Elements, Product Information.
URL https://www.dupont.com/content/dam/dupont/amer/us/en/water-solutions/public/documents/en/45-D01696-en.pdf

[40] C. Y. Tang, T. Chong, A. G. Fane, Colloidal interactions and fouling of NF and RO membranes: A review, Advances in Colloid and Interface Science 164 (1-2) (2011) 126–143. doi:10.1016/j.cis.2010.10.007.

[41] J. Tang, J. Li, J. J. Vlassak, Z. Suo, Adhesion between highly stretchable materials, Soft Matter 12 (4) (2016) 1093–1099. doi:10.1039/C5SM02305J.

[42] S. P. Timoshenko, S. Woinowsky-Krieger, Theory of plates and shells, McGraw-hill, 1959.

[43] D. Rouby, P. Reynaud, Fatigue behaviour related to interface modification during load cycling in ceramic-matrix fibre composites, Composites Science and Technology 48 (1-4) (1993) 109–118. doi:10.1016/0266-3538(93)90126-2.

[44] T. Walander, A. Eklind, T. Carlberger, U. Stigh, Fatigue damage of adhesive layers–experiments and models, Procedia Materials Science 3 (2014) 829–834. doi:10.1016/j.mspro.2014.06.135.

[45] I. A. Ashcroft, Fatigue load conditions, Handbook of Adhesion Technology (2018) 941–973.

[46] K. Golovin, A. Dhyani, M. Thouless, A. Tuteja, Low–interfacial toughness materials for effective large-scale deicing, Science 364 (6438) (2019) 371–375. doi:10.1126/science.aav1266.

[47] M. S. Atab, A. Smallbone, A. Roskilly, An operational and economic study of a reverse osmosis desalination system for potable water and land irrigation, Desalination 397 (2016) 174 – 184. doi:10.1016/j.desal.2016.06.020.

[48] DOW FILMTEC Membranes, Product Information.
URL https://www.dupont.com/content/dam/Dupont2.0/Products/water/literature/609-00438.pdf

[49] DOW FILMTEC BW30-365 Element, Product Information.
URL https://www.dupont.com/content/dam/Dupont2.0/Products/water/literature/609-00153.pdf

[50] S. Lattemann, T. Höpner, Seawater desalination: Impacts of brine and chemical discharge on the marine environment, Balaban Desalination Publications L'Aquila, Italy, 2003.

[51] Q. J. Wei, R. K. McGovern, J. H. Lienhard, Saving energy with an optimized two-stage reverse osmosis system, Environ. Sci.: Water Res. Technol. 3 (2017) 659–670. doi:10.1039/C7EW00069C.

[52] K. H. Mistry, H. A. Hunter, J. H. Lienhard, Effect of composition and nonideal solution behavior on desalination calculations for mixed electrolyte solutions with comparison to seawater, Desalination 318 (2013) 34 – 47. doi:10.1016/j.desal.2013.03.015.

[53] E. W. Tow, D. M. Warsinger, A. M. Trueworthy, J. Swaminathan, G. P. Thiel, S. M. Zubair, A. S. Myerson, J. H. Lienhard, Comparison of fouling propensity between reverse osmosis, forward osmosis, and membrane distillation, Journal of Membrane Science 556 (2018) 352 – 364. doi:10.1016/j.memsci.2018.03.065.

[54] GWI DesalData Cost Estimator, https://www.desaldata.com/cost_estimator, accessed: 2019-05-21.